ACS Catalysis

pubs.acs.org/acscatalysis

Research Article

# A Highly Reactive Chromium(V)−Oxo TAML Cation Radical Complex in Electron Transfer and Oxygen Atom Transfer Reactions

Young Hyun Hong,[⊥] Yuri Jang,[⊥] Roman Ezhov, Mi Sook Seo, Yong-Min Lee, Bhawana Pandey, Seungwoo Hong, Yulia Pushkar,* Shunichi Fukuzumi,* and Wonwoo Nam*

**Cite This:** *ACS Catal.* 2021, 11, 2889−2901

Read Online

ACCESS | Metrics & More | Article Recommendations | Supporting Information

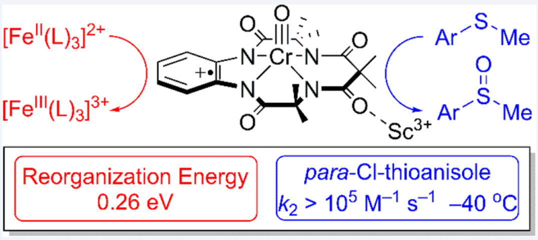

**ABSTRACT:** We report the synthesis, characterization, and electron-transfer (ET) oxidation reactivity of a chromium(V)−oxo TAML cation radical complex binding $Sc^{3+}$ ion, $\{[Cr^V(O)(TAML^{\bullet+})]\text{-}Sc^{3+}\}^{3+}$ (**2**-Sc). Its precursors, such as $[Cr^V(O)(TAML)]^-$ (**1**) and $\{[Cr^V(O)(TAML)]\text{-}Sc^{3+}\}^{2+}$ (**1**-Sc), were also characterized spectroscopically and/or structurally. In ET and oxygen atom transfer (OAT) reactions, while **1** and **1**-Sc were sluggish oxidants, **2**-Sc was a highly reactive oxidant with an extremely small reorganization energy. For example, in ET oxidation reactions, nanosecond laser-induced transient absorption measurements were performed to examine the fast ET from electron donors (e.g., ferrocene derivatives) to **2**-Sc, affording a small reorganization energy ($\lambda$ = 0.26 eV) of ET, which is even much smaller than the $\lambda$ values reported in the ET reduction of heme Compound I (Cpd I) models and non-heme metal−oxo complexes. Such a small reorganization energy is ascribed to the TAML ligand centered ET reduction of **2**-Sc. The $\lambda$ value of 0.26 eV was also obtained in the electron self-exchange reaction between **2**-Sc and **1**-Sc. In OAT reactions, the rate constants of the sulfoxidation of thioanisole derivatives by **2**-Sc at −40 °C were much greater than those reported in the oxidation of thioanisoles by heme Cpd I and non-heme metal−oxo complexes. The reactivity of **2**-Sc in hydrogen atom transfer (HAT) reactions is also discussed briefly. To the best of our knowledge, this Cr(V)-oxo TAML cation radical complex binding $Sc^{3+}$ ion, $\{[Cr^V(O)(TAML^{\bullet+})]\text{-}Sc^{3+}\}^{3+}$, with an extremely small reorganization energy is one of the most powerful high-valent metal−oxo oxidants in ET and OAT reactions.

**KEYWORDS:** *electron transfer, oxygen atom transfer, chromium(V)-oxo complex, redox-inactive metal ion, reorganization energy*

## ■ INTRODUCTION

High-valent iron−oxo species have been invoked as key intermediates in oxidation reactions by iron-containing enzymes and their model compounds, such as in cytochrome P450 and iron porphyrin systems.[1−5] For example, iron(IV)−oxo porphyrin $\pi$-cation-radical species, referred to as Compound I (Cpd I), exhibit high reactivity in electron-transfer (ET) oxidation reactions because of the small reorganization energy ($\lambda$) of the porphyrin ligand centered ET reduction, in comparison to the large reorganization energy of the metal-centered ET reduction of iron(IV)−oxo porphyrin species, referred to as Compound II (Cpd II).[6] Very recently, $\lambda$ values of ET reduction of Cpd I model complexes were determined to be 1.0−1.2 eV,[7] which are much smaller than those of metal-centered ET reduction of synthetic non-heme Fe(IV)−oxo and Mn(IV)−oxo complexes of 2.37−2.74 and 2.24−2.27 eV, respectively.[8−10] The large $\lambda$ values of the metal-centered reduction of the Fe(IV)−oxo and Mn(IV)−oxo complexes result from the structural change during ET due to the d$\sigma$ character of the lowest unoccupied molecular orbital (LUMO).[6,11] In contrast, a small $\lambda$ value of ET reduction would be expected if the LUMO has d$\pi$ character. Indeed, a relatively small $\lambda$ value was reported for the metal-centered ET reduction of a chromium(V)−oxo complex, in which the LUMO possesses d$\pi$ character.[11] If the oxidation of a Cr(V)−oxo complex further occurs at the supporting ligand, the one-electron-oxidized Cr(V)−oxo species, which has the formal oxidation state of Cr(VI), would exhibit a much higher ET oxidation reactivity with a much smaller reorganization energy.

Recently, a couple of high-valent metal−oxo complexes with a metal oxidation state of V with a one-electron-oxidized ligand have been successfully synthesized, such as the Mn(V)−oxo corrolazine cation radical $[Mn^V(O)(Cz^{\bullet+})]^{2+}$ [12] and Mn(V)−oxo tetraamido macrocyclic ligand (TAML) cation radical $[Mn^V(O)(TAML^{\bullet+})]$.[13] More recently, a couple of high-valent metal−imido complexes with a metal oxidation state of V with a one-electron-oxidized ligand have been successfully synthesized, $[Mn^V(N\text{-}Mes)(TAML^{\bullet+})]$[14] and $[Fe^V(NTs)\text{-}$

**Received:** January 7, 2021
**Revised:** January 29, 2021

ACS Publications

https://dx.doi.org/10.1021/acscatal.1c00079
*ACS Catal.* 2021, 11, 2889−2901

(TAML$^{\bullet+}$)],[15] and the ET and redox reactivity of the latter intermediate with a reorganization energy of 1.0 eV was reported.[15] However, the ET oxidation reactivity of these metal−oxo complexes with a metal oxidation state of V with a one-electron-oxidized ligand has never been explored previously.

Herein, we report the synthesis and characterization of a Cr(V)−oxo TAML cation radical complex binding $Sc^{3+}$ ion, $\{[Cr^{V}(O)(TAML^{\bullet+})]\text{-}Sc^{3+}\}^{3+}$ (**2**-Sc); **2**-Sc was generated by the ET oxidation of $\{[Cr^{V}(O)(TAML)]\text{-}Sc^{3+}\}^{2+}$ (**1**-Sc) (Scheme 1). The ET and redox reactivity of **2**-Sc was then examined using nanosecond laser-induced transient absorption spectroscopy. The rate constant of ET from **2**-Sc to $[Fe^{II}(Ph_2\text{-}phen)_3]^{2+}$ was determined to be $[1.6(1)] \times 10^{10}$ $M^{-1}$ $s^{-1}$ at 25 °C (Scheme 1), which is the largest value ever reported in ET reactions by high-valent metal−oxo complexes, including Cpd I models. Such a high oxidation reactivity of **2**-Sc was ascribed to the extremely small reorganization energy ($\lambda$ = 0.26 eV) of the TAML ligand centered ET reduction of **2**-Sc (Scheme 1), which is even much smaller than the $\lambda$ values reported in the ET reduction of Cpd I model complexes.[6,7,16]

**Scheme 1. Synthesis and Oxidation Reactivity of $[Cr^{V}(O)(TAML^{+\bullet})]\text{-}Sc^{3+}$ (2-Sc)**

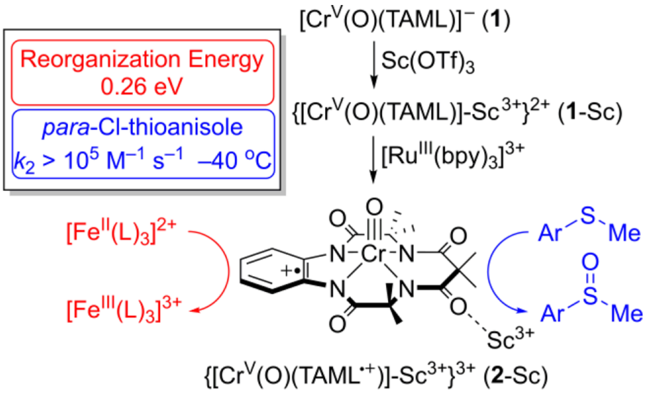

## RESULTS AND DISCUSSION

We first report the synthesis, spectroscopic and/or structural characterization, and DFT-optimized structures of $[Cr^{V}(O)(TAML)]^{-}$ (**1**), $\{[Cr^{V}(O)(TAML)]\text{-}Sc^{3+}\}^{2+}$ (**1**-Sc), and $\{[Cr^{V}(O)(TAML^{\bullet+})]\text{-}Sc^{3+}\}^{3+}$ (**2**-Sc).

**$[Cr^{V}(O)(TAML)]^{-}$ (1).** The room-temperature-stable chromium(V)−oxo TAML complex $[Cr^{V}(O)(TAML)]^{-}$ (**1**) was synthesized (see the Experimental Section) and characterized with various spectroscopic techniques, such as resonance Raman spectroscopy (rRaman), cold-spray ionization mass spectrometry (CSI-MS), electron paramagnetic resonance (EPR), X-ray absorption spectroscopy (XAS), and X-ray crystallography. First, the UV−vis spectrum of **1** exhibited a broad absorption band at 370 nm ($\varepsilon$ = 2500 $M^{-1}$ $cm^{-1}$) in $CH_3CN$ at 25 °C (Figure 1a). The CSI-MS spectrum of **1** in a negative mode revealed one prominent ion peak at a mass to charge ($m/z$) ratio of 438.2 (Figure 1b), whose mass and isotope distribution patterns correspond to $[Cr^{V}(O)(TAML)]^{-}$ (calculated $m/z$ 438.1). Isotopically labeled **1**-$^{18}O$ afforded a mass peak at 440.2 corresponding to $[Cr^{V}(^{18}O)(TAML)]^{-}$ (calculated $m/z$ 440.1) (Figure 1b, inset). In rRaman experiments, upon 441.7 nm excitation, **1** exhibited an isotopically sensitive band at 981 $cm^{-1}$, which shifted to 942 $cm^{-1}$ upon $^{18}O$ substitution (Figure 1c). The observed stretching frequency at 981 $cm^{-1}$ indicates a Cr−O triple bond (*vide infra*).[11a,17] The $\Delta\nu(^{16}O{-}^{18}O)$ value of 39 $cm^{-1}$ is consistent with the calculated $\Delta\nu(^{16}O{-}^{18}O)$ value of 43 $cm^{-1}$ from Hook's law for a diatomic Cr−O oscillator. An EPR spectrum of **1** was recorded in $CH_3CN$ at −30 °C, affording signals centered at $g$ = [2.0003, 1.9818, 1.9645] with the hyperfine coupling tensor $A_{Cr}$ = [7.6, 7.7, 7.6] MHz (Figure 1c, inset), which is characteristic of $d^1$ $Cr^{V}$ complexes.[18] Figure 2a shows the X-ray absorption near-edge structure (XANES) of **1**. The edge position is consistent with the $Cr^{V}$ oxidation state, and the strong pre-edge feature at ∼5992 eV originates from the strong Cr−O orbital hybridization across the short Cr≡O bond.[19] Two peaks in the extended X-ray absorption fine structure (EXAFS) indicate

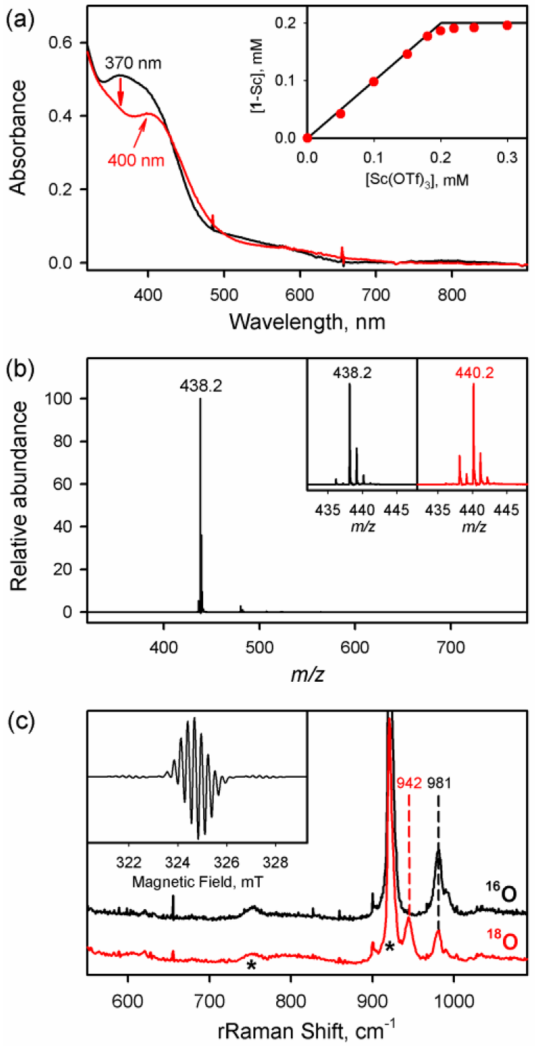

**Figure 1.** (a) UV−vis spectrum of **1** (0.20 mM, black line) and the spectral change observed in the reaction of **1** (0.20 mM, black line) and $Sc(OTf)_3$ (0.3 mM) in $CH_3CN$ at 25 °C for the formation of **1**-Sc (red line). The inset shows the plot of **1**-Sc vs the concentration of $Sc(OTf)_3$ upon addition of $Sc(OTf)_3$ (0−0.30 mM) to **1** (0.20 mM). (b) Negative mode CSI-MS spectrum of **1** in $CH_3CN$ at −40 °C. Insets show the observed isotope distribution patterns for **1**-$^{16}O$ (left panel) and **1**-$^{18}O$ (right panel). (c) rRaman spectra of **1**-$^{16}O$ (4.0 mM, black line) and **1**-$^{18}O$ (4.0 mM, red line) in $CH_3CN$ at −40 °C. The peaks marked with asterisks are from the solvent. The inset shows the X-band CW-EPR spectrum of **1** (0.20 mM) recorded at −30 °C.

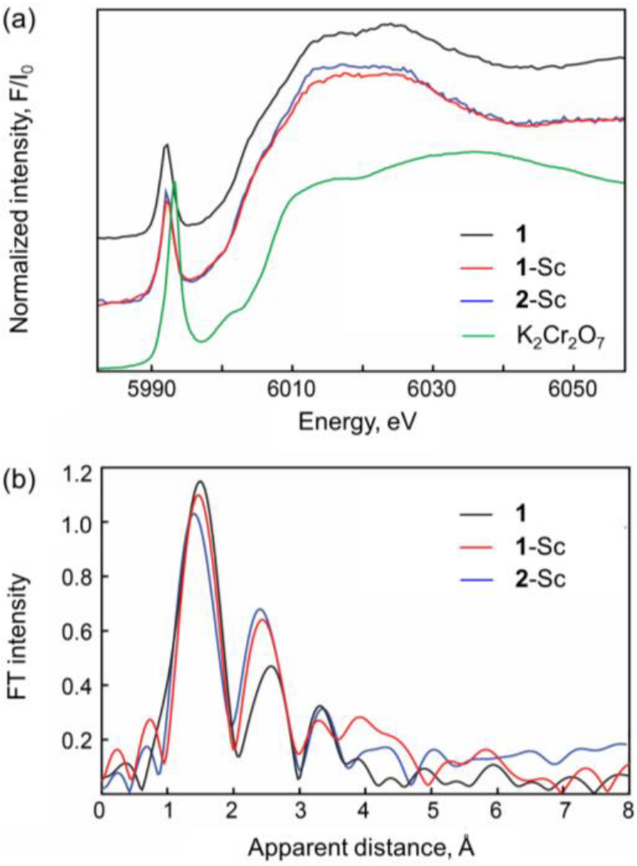

**Figure 2.** (a) XAS data for **1** (black line), **1**-Sc (red line), **2**-Sc (blue line), and $K_2Cr_2O_7$ (green line). (b) Fourier-transformed EXAFS for **1** (black line), **1**-Sc (red line), and **2**-Sc (blue line).

first Cr—N and Cr—O and second Cr—C coordination shells (Figure 2b; see also Table S1 in the Supporting Information for fit results). The Cr—O distance is ~1.56 Å (Table S1), which is in good agreement with the X-ray diffraction (XRD) data of **1** (*vide infra*). Finally, single crystals suitable for an X-ray crystal structure analysis were obtained, and the crystallographic analysis of the single crystals revealed that **1** is a monomeric five-coordinate Cr$^{V}$(O) species, [Cr$^{V}$(O)(TAML)]$^{-}$, with a short Cr—O distance of 1.569 Å (Figure 3; see Tables S2 and S3 in the Supporting Information for the crystallographic data); the short Cr—O distance is consistent with the rRaman data and the EXAFS data obtained in this study as well as those reported for a number of Cr$^{V}$—O complexes.[17b,18a,20]

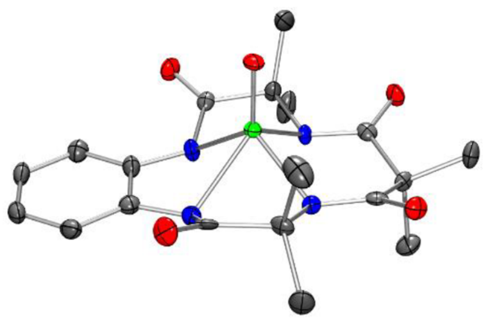

**Figure 3.** X-ray crystal structure of [Cr$^{V}$(O)(TAML)]$^{-}$ (**1**) showing 50% probability ellipsoids. Tetraphenylphosphonium ion and hydrogen atoms are omitted for clarity. Color code for atoms: Cr, green; O, red; N, blue; C, gray.

**{[Cr$^{V}$(O)(TAML)]-Sc$^{3+}$}$^{2+}$ (1-Sc).** Addition of 5 equiv of Sc(OTf)$_3$ (OTf$^{-}$ = $CF_3SO_3^{-}$) to a $CH_3CN$ solution of **1** at 25 °C resulted in an UV—vis spectral change (Figure 1a, red line). The spectral titration experiment afforded a binding constant of $4.5 \times 10^5$ M$^{-1}$ (Figure S1 in the Supporting Information). The EPR spectrum of **1**-Sc, recorded at −30 °C, exhibited signals at $g$ = 1.9818 (Figure S2a in the Supporting Information), which is virtually the same as that of **1** (Figure 1b). The CSI-MS spectrum of **1**-Sc in positive mode exhibited one prominent ion peak at $m/z$ 930.0 (Figure S2b in the Supporting Information), whose mass and isotope distribution patterns correspond to [Cr$^{V}$(O)(TAML)(Sc)(OTf)$_3$]$^{-}$ (calculated $m/z$ 929.9). When **1**-Sc-$^{18}$O was prepared with **1**-$^{18}$O, a mass peak corresponding to [Cr$^{V}$($^{18}$O)(TAML)(Sc)(OTf)$_3$]$^{-}$ (calculated $m/z$ 931.9) appeared at $m/z$ 932.0 (Figure S2b, inset). In rRaman experiments, upon 441.7 nm excitation, **1**-Sc exhibited an isotopically sensitive band at 988 cm$^{-1}$ (Figure S2c in the Supporting Information), which is red-shifted by 7 cm$^{-1}$ in comparison to **1**. With $^{18}$O-substituted **1**-Sc-$^{18}$O, a band appeared at 948 cm$^{-1}$ (Figure S2c in the Supporting Information), and the observed $\Delta\nu$($^{16}$O—$^{18}$O) value of 40 cm$^{-1}$ is in good agreement with the calculated $\Delta\nu$($^{16}$O—$^{18}$O) value of 43 cm$^{-1}$ for a diatomic Cr—O oscillator. Such a red shift of the $\nu$(Cr—O) values in **1**-Sc and **1**-Sc-$^{18}$O suggests that the Sc$^{3+}$ ion is bound not to the Cr—oxo moiety but to the carbonyl group of the ligand (*vide infra*), since we would expect to see a blue-shifted rRaman band if the Sc$^{3+}$ ion is bound to the Cr—oxo moiety, as has been shown in an iron(IV)—oxo porphyrin complex[21] as well as in Mn(V)—oxo TAML and Mn(V)—oxo TAML binding Sc$^{3+}$ ion.[22] The XANES of **1**-Sc is indistinguishable from that of **1**, and no changes in the shapes of edge or pre-edge features are noted (Figure 2a). This indicates that Cr—O bonding was not affected by the binding of the Sc$^{3+}$ ion. EXAFS fits indicate a slightly shorter Cr—O bond ~1.55 Å (Table S1 and Figures S3 and S4 in the Supporting Information). On the basis of the spectroscopic characterization of **1**-Sc, we propose that the Cr(V)—oxo complex binds the Sc$^{3+}$ ion at the carbonyl group of the TAML ligand, as proposed in a Mn(V)—oxo TAML complex binding Sc$^{3+}$ ion.[22]

**{[Cr$^{V}$(O)(TAML$^{\bullet+}$)]-Sc$^{3+}$}$^{3+}$ (2-Sc).** When **1**-Sc was reacted with a one-electron oxidant, such as [Ru$^{III}$(bpy)$_3$]$^{3+}$ (bpy = 2,2′-bipyridine), and cerium(IV) ammonium nitrate (CAN) in $CH_3CN$ at −40 °C, we observed an immediate UV—vis spectral change, showing two broad absorption bands at 615 nm ($\varepsilon$ = 5500 M$^{-1}$ cm$^{-1}$) and 800 nm ($\varepsilon$ = 4600 M$^{-1}$ cm$^{-1}$) (Figure 4a).[23] The spectral titration experiments revealed that 1 equiv of the one-electron oxidant (e.g., [Ru$^{III}$(bpy)$_3$]$^{3+}$) was required for the formation of the new intermediate, denoted **2**-Sc (Figure 4a, inset). While the X-band EPR spectrum of **1**-Sc exhibited signals centered at $g$ = 1.9818 (*vide supra*), **2**-Sc was EPR-silent (Figure 4b), suggesting that **2**-Sc is a one-electron-oxidized species of **1**-Sc. Since **2**-Sc was highly unstable under the conditions of CSI-MS (e.g., a thermal instability) and rRaman (e.g., an instability at high concentration), we were not able to obtain these informative spectral data. However, we were able to characterize **2**-Sc using cryogenic Cr K-edge X-ray absorption spectroscopy (XAS). Figure 2a shows the comparison of the XANES of **1**, **1**-Sc, and **2**-Sc. The Cr K-edge of **2**-Sc exhibits no shift in comparison with those of **1** and **1**-Sc, indicating that the oxidation state of Cr in **2**-Sc

https://dx.doi.org/10.1021/acscatal.1c00079
ACS Catal. 2021, 11, 2889−2901

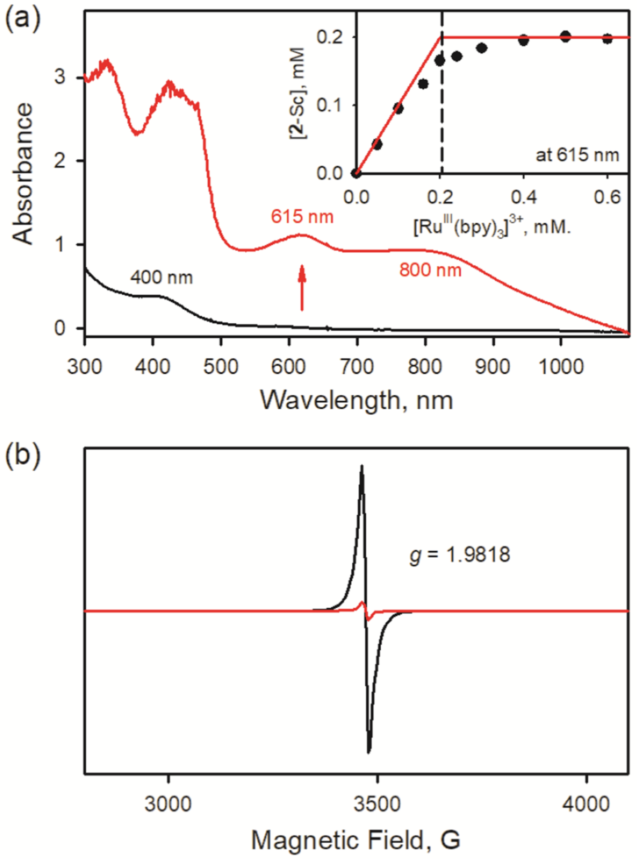

**Figure 4.** (a) UV−vis spectral changes observed in the reaction of **1**-Sc (0.20 mM, black line) and [Ru$^{III}$(bpy)$_3$]$^{3+}$ (0.60 mM) in $CH_3CN$ at −40 °C for the formation of **2**-Sc (red line). The inset shows a plot of **2**-Sc produced vs the concentration of [Ru$^{III}$(bpy)$_3$]$^{3+}$ upon addition of [Ru$^{III}$(bpy)$_3$]$^{3+}$ (0−0.60 mM) to **1**-Sc (0.20 mM). (b) X-band CW-EPR spectra of **1**-Sc (0.20 mM; black line) and **2**-Sc (0.20 mM; red line) recorded in $CH_3CN$ at 77 K.

remains as Cr$^V$. Neither addition of Sc(OTf)$_3$ nor oxidation changes the edge position or pre-edge structure, indicating no change in Cr$^V$ oxidation state or Cr−O bonding. As shown in Figure 2b, EXAFS does not show any additional Cr−Sc interactions either, suggesting that the Sc binding might happen away from the Cr center (also see Table S1 and Figures S3 and S4 in the Supporting Information for the fit results). The Cr−O distance further shortens to ∼1.53 Å. On the basis of the spectroscopic characterization of **2**-Sc, we therefore conclude that **2**-Sc is a Cr(V)−oxo TAML cation radical complex binding Sc$^{3+}$ ion at the carbonyl group of the TAML ligand, {[Cr$^V$(O)(TAML$^{•+}$)]-Sc$^{3+}$}$^{3+}$.

**DFT-Optimized Structures.** Density functional theory (DFT) calculations have been performed on the Cr−oxo complexes **1**, **1**-Sc, and **2**-Sc (Tables S4−S9 in the Supporting Information). For **1**, a doublet state ($S = 1/2$) has been found to be the ground state with an excited quartet state lying higher at 31.97 kcal/mol (Tables S4 and S5 in the Supporting Information). The optimized structure of the ground state ($^2$**1**) shows square-pyramidal geometry around the Cr center with a Cr−O$^a$ bond distance of 1.552 Å (Figure 5). This short bond length is attributed to the strong interaction between chromium and the oxo moiety, which suggests a triple-bond character of the Cr−O bond and is in good agreement with the experimental rRaman, EXAFS, and XRD (1.569 Å) results.

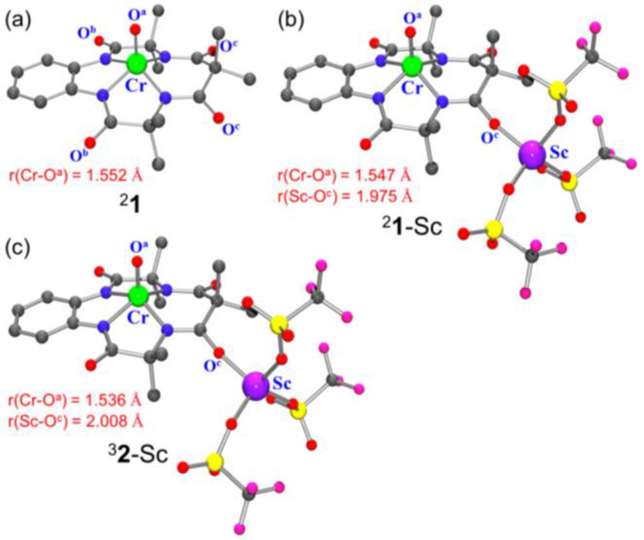

**Figure 5.** DFT-optimized structures of $^2$**1**, $^2$**1**-Sc, and $^3$**2**-Sc.

From the optimized structure of **1**, it is evident that there are three possible Sc$^{3+}$ binding sites to the oxygen atoms (O$^a$, O$^b$, and O$^c$; see Figure 5a for the labeling of oxygen atoms). DFT calculations on **1**-Sc reveal that Sc$^{3+}$ ion binding at the O$^c$ position is more favorable than binding at O$^a$ and O$^b$ by 11.03 and 2.58 kcal/mol, respectively (Scheme S1 and Table S6 in the Supporting Information). In the case of Sc$^{3+}$ ion binding at O$^c$, the calculated Cr−O$^a$ and Sc$^{3+}$−O$^c$ bond distances are found to be 1.547 and 1.975 Å, respectively (Figure 5b). In contrast to the Sc$^{3+}$ ion binding at O$^c$, binding to the oxo moiety (i.e., O$^a$) leads to the elongation of the Cr−O bond distance from 1.547 to 1.654 Å, resulting in the weakening of the Cr−O bond in comparison to the structure of the Sc$^{3+}$ ion binding at O$^c$ (and/or O$^b$; Table S7 in the Supporting Information). These results reinforce the rRaman and EXAFS experimental findings, thus evidencing the Sc$^{3+}$ ion binding to O$^c$ in the TAML ligand instead of the oxo moiety (i.e., O$^a$).

Further, the one-electron-oxidized complex **2**-Sc has also been explored for all nine possible spin states originating from the various electronic arrangements in the complex. Like **1**-Sc, for **2**-Sc, Sc$^{3+}$ ion binding at O$^c$ is predicted to be the most favorable (Table S8 in the Supporting Information). The triplet state of the Sc$^{3+}$ ion binding at O$^c$ has been assigned as a ground state, which has a lower energy in comparison to those of the triplet state of the Sc$^{3+}$ ion binding at O$^a$ and O$^b$ (12.83 and 5.06 kcal/mol, respectively; Table S8 in the Supporting Information). The energy gap between the triplet state $^3$**2**-Sc-O$^c$ and the open shell singlet (OSS) $^1$**2**-Sc-O$^c_{OSS}$ is 0.2 kcal/mol in electronic energy, which does not allow for differentiation beyond the error margins (Table S8 in the Supporting Information). This is due to the fact that the only difference between these two species is whether there is an $\alpha$-spin or a $\beta$-spin on the ligand. The small energy difference thus signifies the strength of the antiferromagnetic coupling. As there are no meaningful geometrical differences between these two species, a definite spin state determination has to come from experiments, whenever possible. Unfortunately, due to the instability of **2**-Sc, the exact spin state of **2**-Sc ($S = 0$ or 1) could not be determined by the Evans method of NMR. All of the spin states corresponding to the closed-shell singlet (CSS) are lying higher in energy than those of the triplet ground state. Similar to the case for **1**-Sc, the Sc$^{3+}$ ion binding at O$^c$ for **2**-Sc is thus found to be more favorable than binding at $O^a$ and $O^b$. In the case of $Sc^{3+}$ ion binding at $O^c$, the calculated Cr−$O^a$ and Sc−$O^c$ bond distances are found to be 1.536 and 2.008 Å, respectively. Binding of the $Sc^{3+}$ ion in **1**-Sc or **2**-Sc does not cause significant changes in the Cr−O bond distances, endorsing the fact that the $Sc^{3+}$ ion binds to the oxygen atom of the carbonyl group in TAML ligand, not to the oxo moiety, which is in good agreement with the results obtained from the analysis of the rRaman and XANES/EXAFS data for **1**, **1**-Sc, and **2**-Sc.

With the well-characterized Cr(V)−oxo species in hand, we studied the ET oxidation reactivity of **1**, **1**-Sc, and **2**-Sc.

**Electron-Transfer Reactivity of 2-Sc.** Nanosecond laser-induced transient absorption measurements were performed to examine the fast ET from electron donors to $\{[Cr^V(O)(TAML^{\bullet+})]\text{-}Sc^{3+}\}^{3+}$ (**2**-Sc), because the ET rate was too fast to follow using a stopped-flow technique even at −40 °C. First, **2**-Sc was generated by ET from **1**-Sc to the triplet excited state of 2,3-dichloro-5,6-dicyano-*p*-benzoquinone ($^3DDQ^*$) (Figure 6a), where a transient absorption band due to **2**-Sc ($\lambda_{max}$ = 615 nm) was observed upon laser photoexcitation, being overlapped with the transient absorption band due to $DDQ^{\bullet-}$ ($\lambda_{max}$ = 590 nm).[24,25] Highly exergonic ET from **1**-Sc ($E_{ox}$ vs SCE = 1.22 V) (Figure S5 in the Supporting Information) to $^3DDQ^*$ ($E_{red}$ vs SCE = 3.1 V)[24,25] was expected to occur at the diffusion rate constant (e.g., $2.0 \times 10^{10}$ $M^{-1}$ $s^{-1}$). Indeed, the formation of **2**-Sc via ET from **1**-Sc (0.010 mM) to $^3DDQ^*$ occurred rapidly, followed by the decay of the transient absorption band at 615 nm due to **2**-Sc by ET from $[Fe^{II}(5\text{-Cl-phen})_3]^{2+}$ to **2**-Sc (inset of Figure 6b). The products formed in ET from $[Fe^{II}(5\text{-Cl-phen})_3]^{2+}$ to **2**-Sc were analyzed by EPR, showing the formation of $[Fe^{III}(5\text{-Cl-phen})_3]^{3+}$ and **1**-Sc (Figure S6 in the Supporting Information). The pseudo-first-order rate constant increased linearly with an increasing concentration of $[Fe^{II}(5\text{-Cl-phen})_3]^{2+}$ (Figure S7 in the Supporting Information). The second-order rate constant ($k_{et}$) of ET from $[Fe^{II}(5\text{-Cl-phen})_3]^{2+}$ to **2**-Sc was determined from the plot of the pseudo-first-order rate constant vs concentration of $[Fe^{II}(5\text{-Cl-phen})_3]^{2+}$ (Figure S7c in the Supporting Information). Similarly, the $k_{et}$ values of ET from $[Fe^{II}(Ph_2\text{-phen})_3]^{2+}$ and $[Fe^{II}(phen)_3]^{2+}$ to **2**-Sc were determined, as given in Table 1 (see also Figure S8 in the Supporting Information), together with the $E_{ox}$ values of one-electron donors and the driving force of ET ($-\Delta G_{et}$ (in eV) = $e(E_{red} - E_{ox})$, where $e$ is the elementary charge). It should be noted that no ET from coordinatively saturated $Fe^{II}$ complexes (i.e., $[Fe^{II}(Ph_2\text{-phen})_3]^{2+}$, $[Fe^{II}(phen)_3]^{2+}$, and $[Fe^{II}(5\text{-Cl-phen})_3]^{2+}$) to **1** and **1**-Sc occurs, since the one-electron-reduction potentials ($E_{red}$ vs SCE) of **1** and **1**-Sc, −0.53 and 0.51 V, respectively (see Figures S9 and S10 in the Supporting Information), are much smaller than the one-electron-oxidation potentials ($E_{ox}$) of the coordinatively saturated $Fe^{II}$ complexes.

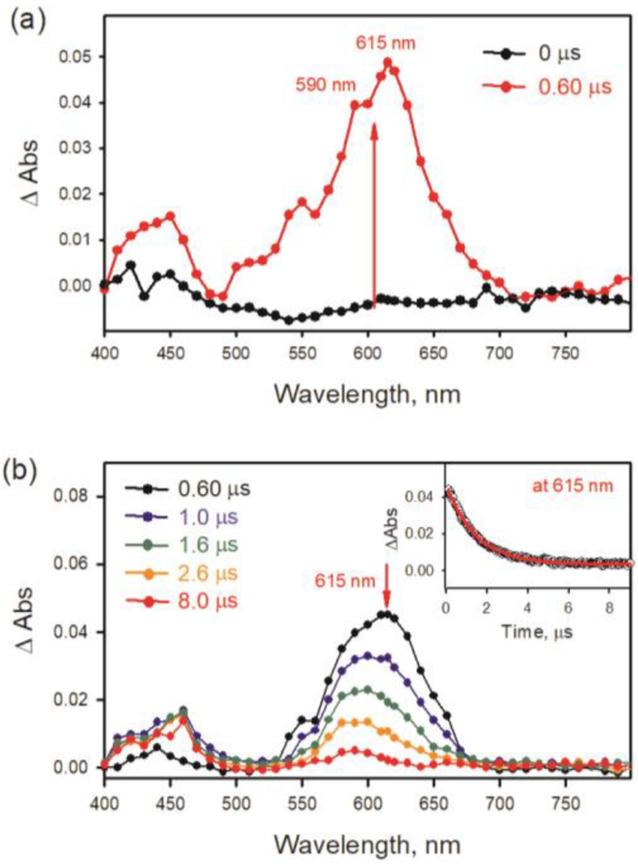

**Figure 6.** (a) Transient absorption spectral changes observed in electron transfer from **1**-Sc (0.010 mM) to the triplet excited state of DDQ ($^3DDQ^*$; 0.10 mM) after laser excitation at 355 nm in deaerated $CH_3CN$ at 25 °C to produce **2**-Sc ($\lambda_{max}$ = 615 nm) and $DDQ^{\bullet-}$ ($\lambda_{max}$ = 590 nm). (b) Transient absorption spectral changes observed in the reaction of **2**-Sc and $[Fe^{II}(5\text{-Cl-phen})_3]^{2+}$ (50 $\mu$M) at 25 °C. **2**-Sc was produced *in situ* by an electron transfer from **1**-Sc (0.010 mM) to the triplet excited state of DDQ ($^3DDQ^*$) after laser excitation at 355 nm of a $CH_3CN$ solution of DDQ (0.10 mM). The inset shows the time profile of absorbance monitored at 615 nm due to **2**-Sc.

**Table 1. One-Electron-Oxidation Potentials ($E_{ox}$) of One-Electron Donors and *para*-Substituted Thioanisoles and Rate Constants ($k_{et}$) of Electron Transfer from One-Electron Donors to 2-Sc and Sulfoxidation of *para*-Substituted Thioanisoles by 2-Sc in $CH_3CN$ at 25 °C**

| one-electron donor | $E_{ox}$ vs SCE, V | $k_2$, $10^{10}$ $M^{-1}$ $s^{-1}$ | $-\Delta G_{et}$ |
|---|---|---|---|
| $[Fe^{II}(Ph_2\text{-phen})_3]^{2+}$ | 1.02 | 1.6(1) | 0.20 |
| $[Fe^{II}(phen)_3]^{2+}$ | 1.07 | 1.3(1) | 0.15 |
| $[Fe^{II}(5\text{-Cl-phen})_3]^{2+}$ | 1.17 | 1.0(1) | 0.05 |

According to the Marcus theory of outer-sphere ET, the driving force ($-\Delta G_{et}$) dependence of $k_{et}$ is given by eqs 1 and 2 (Figure 7)

$$1/k_{et} = 1/k_{diff} + 1/(Z \exp[-\Delta G^{\ddagger}/(k_B T)]) \tag{1}$$

$$\Delta G^{\ddagger} = (\lambda/4)(1 + \Delta G_{et}/\lambda)^2 \tag{2}$$

where $k_{diff}$ is the diffusion rate constant, $\Delta G^{\ddagger}$ is the activation Gibbs energy, and $\lambda$ is the reorganization energy of ET.[26] Although the number of data points is limited, the $\lambda$ value can be determined with a relatively small experimental error to be 0.26(2) eV (Figure 7, red line), because the data points include the $k_{et}$ value with a small $\Delta G_{et}$ value (note that $\Delta G^{\ddagger} = \lambda/4$ when $\Delta G_{et} = 0$). The validity of the small $\lambda$ value was confirmed by an independent determination of the $\lambda$ value with use of EPR line width alternation (*vide infra*). The $\lambda$ value of 0.26 eV is much smaller than those determined in the ET reduction of synthetic metal(IV)−oxo complexes (e.g., 2.37−2.74 eV), which is the metal-centered reduction of metal(IV)−

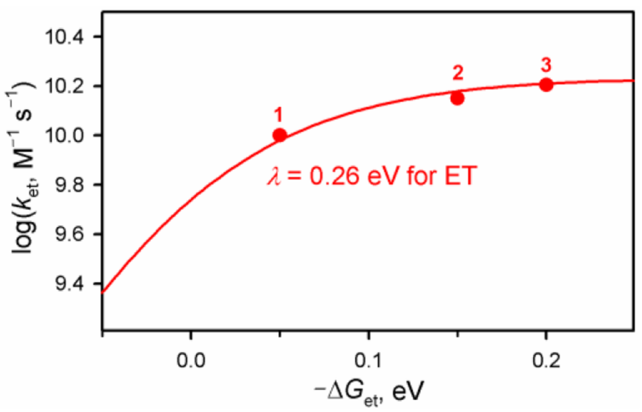

**Figure 7.** Driving force ($-\Delta G_{et}$) dependence of the logarithm of the rate constants (log $k_{et}$) of ET from one-electron donors ((1) [$Fe^{II}$(5-Cl-phen)$_3$]$^{2+}$, (2) [$Fe^{II}$(phen)$_3$]$^{2+}$, and (3) [$Fe^{II}$($Ph_2$-phen)$_3$]$^{2+}$) to **2**-Sc (red circles) in $CH_3CN$ at 25 °C.

oxo species.[8−10] It should be noted that the $\lambda$ value of 0.26 eV is even much smaller than those of the ET reduction of Cpd I model complexes (e.g. ~1.2−1.4 eV), which occurs at the porphyrin ligand center rather than the iron center.[7] The small $\lambda$ value of ET reduction of **2**-Sc may be rationalized by the combination of the small $\lambda$ values of the TAML cation radical ligand-centered ET and the metal-centered reduction of a Cr(V)−oxo complex due to the d$\pi$ character of the LUMO, in contrast to the d$\sigma$ character of the LUMO of Fe(IV)−oxo complexes.[8c,11a,17] Thus, any contribution of the metal-centered reduction to the ligand-centered reduction of metal−oxo complexes results in a much smaller $\lambda$ value of **2**-Sc, in comparison to the Cpd I models.[7] To the best of our knowledge, the present study reports the smallest reorganization energy in the ET reduction of high-valent metal−oxo complexes in heme and non-heme systems investigated so far.

**Electron Self-Exchange between 1-Sc and 2-Sc.** The rate constant of electron self-exchange reaction between **1**-Sc and **2**-Sc (eq 3) was determined by exchange broadening of EPR lines (vide infra).[11b]

$$\mathbf{1}\text{-Sc} + \mathbf{2}\text{-Sc} \rightarrow \mathbf{2}\text{-Sc} + \mathbf{1}\text{-Sc} \quad (3)$$

EPR spectrum of **1**-Sc in $CH_3CN$ was recorded at −30 °C (Figure 8a, black line). The hyperfine splitting constant ($a_{Cr}$) and the maximum slope line width ($\Delta H_{msl}$) were determined by simulating the EPR spectrum (Figure 8a, red line). The $\Delta H_{msl}$ value of **1**-Sc in the absence of **2**-Sc was smaller than that in the presence of **2**-Sc, which was produced by the one-electron oxidation of **1**-Sc by CAN (Figure 8b). The $\Delta H_{msl}$ value increased linearly with an increase in concentration of CAN (Figure 8c). Such line width variations of the EPR spectra can be applied to determine the rate constants of the electron self-exchange reactions between **1**-Sc and **2**-Sc using eq 4

$$k_{ex} = (1.57 \times 10^7)(\Delta H_{msl} - \Delta H^{\circ}_{msl})/(1 - P_i)[\text{CAN}] \quad (4)$$

where $\Delta H_{msl}$ and $\Delta H^{\circ}_{msl}$ are the maximum slope line width of the EPR spectra in the presence and absence of **2**-Sc, respectively, and $P_i$ (~0) is a statistical factor.[27−29] The $k_{ex}$ value was determined to be 9.8 × $10^9$ $M^{-1}$ $s^{-1}$ from the slope of the linear correlation between $\Delta H_{msl}$ and [CAN] (Figure 8c). The reorganization energy ($\lambda$ = 0.26 eV) of the electron self-exchange reaction was then obtained from the $k_{ex}$ value using eq 5

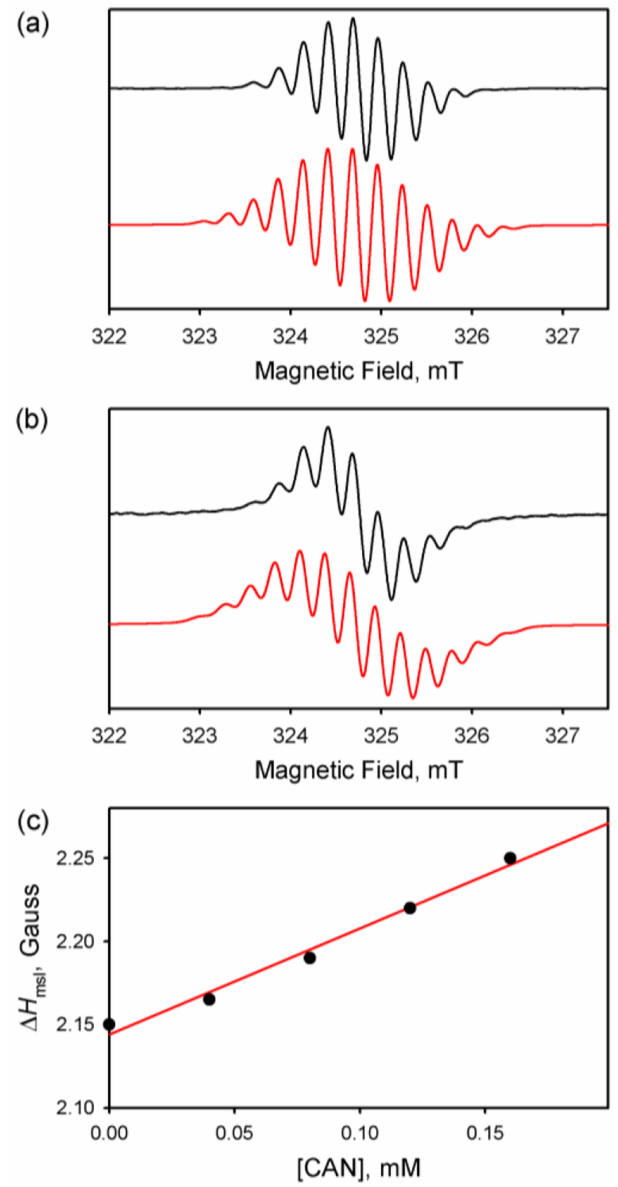

**Figure 8.** (a) Observed (black line) and simulated (red line) EPR spectra of **1**-Sc (0.20 mM) in $CH_3CN$ at −30 °C ($g$ = 1.9818, $a_{Cr}$ = 0.274 mT, $\Delta H_{msl}$ = 0.215 mT). (b) Observed (black line) and simulated (red line) EPR spectra of **1**-Sc(OTf)$_3$ (40 $\mu$M) with **2**-Sc (160 $\mu$M) in $CH_3CN$ at −30 °C ($g$ = 1.9818, $a_{Cr}$ = 0.274 mT, $\Delta H_{msl}$ = 0.225 mT). (c) Plot of $\Delta H_{msl}$ of EPR spectrum of **1**-Sc vs concentration of CAN, which is the same as the concentration of **2**-Sc.

$$k_{ex}^{-1} - k_{diff}^{-1} = Z^{-1} \exp[\lambda/(4k_BT)] \quad (5)$$

where $k_{diff}$ is the diffusion rate constant in $CH_3CN$ (2 × $10^{10}$ $M^{-1}$ $s^{-1}$), agreeing well with the value shown in Figure 7. The delocalization of electrons in the TAML$^{4-}$ ligand in **1**-Sc may result in a small structural change upon the electron-transfer oxidation, leading to the small reorganization energy of the electron-self-exchange between **1**-Sc and **2**-Sc. The reorganization energy of self-exchange between **1** and **2** may be smaller than that between **1**-Sc and **2**-Sc. Without binding of $Sc^{3+}$, however, **2** was very unstable and we were not able to study the ET reactivity. The instability of **2** without binding of $Sc^{3+}$

https://dx.doi.org/10.1021/acscatal.1c00079
ACS Catal. 2021, 11, 2889−2901

has precluded the determination of the one-electron-reduction potential, which can be compared with that of **2**-Sc to determine the change in the binding constants of $Sc^{3+}$ between **1**-Sc and **2**-Sc.

**Sulfoxidation of Thioanisole by 2-Sc.** The reactivity of **2**-Sc in the OAT reactions (i.e., sulfoxidation of *para*-substituted thioanisole derivatives bearing an electron-withdrawing substituent such as *para*-CN-thioanisole) was investigated in $CH_3CN$ at −40 °C; these substrates are less reactive, and the reactions were followed using a stopped-flow spectrophotometer. It should be noted that the OAT rates with thioanisole and *para*-substituted thioanisole derivatives bearing electron-donating substituent such as *para*-MeO-thioanisole and *para*-Me-thioanisole were too fast to follow using a stopped-flow technique even at −40 °C.[30−38] Upon addition of *para*-CN-thioanisole (1.0 mM) to an $CH_3CN$ solution of **2**-Sc at −40 °C, the absorption band at 615 nm due to **2**-Sc decreased with a first-order kinetics profile, giving a first-order rate constant ($k_{obs}$) of 2.8 $s^{-1}$ (Figure S11 in the Supporting Information). The $k_{obs}$ value was in proportion to the *para*-CN-thioanisole concentration to give a second-order rate constant ($k_2$) of [2.8(2)] × $10^3$ $M^{-1}$ $s^{-1}$ at −40 °C. Similarly, the second-order rate constants were determined for other *para*-substituted thioanisole derivatives, such as *para*-$NO_2$-thioanisole, *para*-Br-thioanisole, and *para*-Cl-thioanisole (Table 2; Figure S12 in the Supporting Information).[39,40]

**Table 2. One-Electron-Oxidation Potentials ($E_{ox}$) and Hammett Parameters ($\sigma_p^+$) of *para*-X-Substituted Thioanisoles and Second-Order Rate Constants ($k_2$) of Sulfoxidation of *para*-X-Substituted Thioanisoles by 2-Sc in $CH_3CN$ at −40 °C**

| *para*-X | $E_{ox}$ vs SCE, V | $\sigma_p^+$ | $k_2$, $M^{-1}$ $s^{-1}$ |
|---|---|---|---|
| Cl | 1.37 | 0.11 | 3.1(3) × $10^5$ |
| Br | 1.41 | 0.15 | 2.2(2) × $10^5$ |
| CN | 1.61 | 0.66 | 2.8(2) × $10^3$ |
| $NO_2$ | 1.70 | 0.79 | 2.2(2) × $10^2$ |

When logarithms of the second-order rate constants (log $k_2$) were plotted against the oxidation potentials ($E_{ox}$) of substrates, a good linear correlation was observed with a slope of −9.6 (Figure 9a). In addition, a $\rho$ value of −4.3 was obtained from the Hammett plot of log $k_2$ against $\sigma_p^+$ (Figure 9b). These results demonstrate the electrophilic character of **2**-Sc, as seen in the oxidation of thioanisole derivatives by high-valent metal−oxo complexes.[4,8,10] In the oxidation of thioanisole by **2**-Sc, product analysis revealed that methyl phenyl sulfoxide (PhS(=O)Me) was produced as the sole product with 85(5)% yield on the basis of the amount of **2**-Sc (Figure S13 in the Supporting Information). We also found the formation of $[Cr^V(O)(TAML)]^-$ as the decay product of **2**-Sc (Figure S14 in the Supporting Information). The formation of $[Cr^V(O)(TAML)]^-$ was probably due to the fast oxidation of $[Cr^{III}(TAML)]^-$ by $O_2$. **2**-Sc shows a moderate reactivity in the sulfoxidation reactions, whereas **1** and **1**-Sc are inactive in the sulfoxidation of thioanisole derivatives (Figure S15a,c in the Supporting Information).

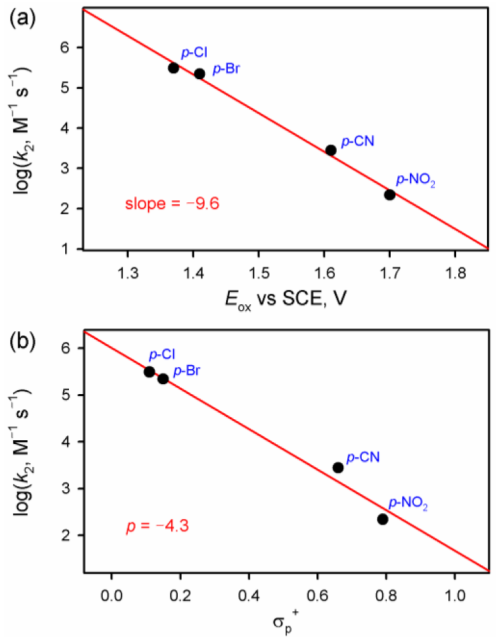

**Figure 9.** Plots of log $k_2$ against (a) one-electron-oxidation potentials ($E_{ox}$ vs SCE) and (b) Hammett parameters ($\sigma_p^+$) of *para*-X-substituted thioanisoles (X = Cl, Br, CN, $NO_2$) for the sulfoxidation of thioanisoles by **2**-Sc in $CH_3CN$ at −40 °C.

The catalytic performance of **2**-Sc was examined in the sulfoxidation of *para*-$NO_2$-thioanisole by $[Ru^{III}(bpy)_3]^{3+}$. $[Ru^{II}(bpy)_3]^{2+}$ was formed with a much faster rate in the catalytic sulfoxidation reaction of *para*-$NO_2$-thioanisole with $[Ru^{III}(bpy)_3]^{3+}$ in the presence of **2**-Sc in comparison with that of the control reaction of *para*-$NO_2$-thioanisole with $[Ru^{III}(bpy)_3]^{3+}$ in the absence of **2**-Sc (Figure S16 in the Supporting Information). The initial rate of the formation of $[Ru^{II}(bpy)_3]^{2+}$ increased with an increase in the concentration of *para*-$NO_2$-thioanisole (Figure S17b in the Supporting Information). In such a case, the initial rate of formation of $[Ru^{II}(bpy)_3]^{2+}$ is given by eq 6

$$\begin{aligned} & d[[Ru^{II}(bpy)_3]^{2+}]/dt \\ & \quad = -2d[\mathbf{2}\text{-Sc}]/dt \\ & \quad = 2k_{ox}[\mathbf{2}\text{-Sc}][para\text{-}NO_2\text{-thioanisole}] \end{aligned} \tag{6}$$

where the initial rate of the production of $[Ru^{II}(bpy)_3]^{2+}$ is twice the decay rate of **2**-Sc, since 2 equiv of $[Ru^{III}(bpy)_3]^{3+}$ is required to regenerate **2**-Sc from the two-electron-reduced product of **2**-Sc in the sulfoxidation reaction and $k_{ox}$ is the second-order rate constant of the sulfoxidation reaction of *para*-$NO_2$-thioanisole by **2**-Sc. The 2$k_{ox}$ value was determined to be [4.5(2)] × $10^2$ $M^{-1}$ $s^{-1}$ from the slope of a plot of the initial rate of formation of $[Ru^{II}(bpy)_3]^{2+}$ vs the concentration of *para*-$NO_2$-thioanisole and the concentration of **2**-Sc (10 μM) (Figure S17c in the Supporting Information). The $k_{ox}$ value (2.3 × $10^2$ $M^{-1}$ $s^{-1}$) obtained from the 2$k_{ox}$ value agreed well with that determined for the sulfoxidation of *para*-$NO_2$-thioanisole by **2**-Sc (Table 2 and Figure S12 in the Supporting Information). The turnover number (TON) for the catalytic sulfoxidation reaction was 28 ± 2 on the basis of **2**-Sc (Figure S18a in the Supporting Information).

**C−H Bond Activation of Alkyl Hydrocarbons by 2-Sc.** The reactivity of $\{[Cr^V(O)(TAML^{\bullet+})]\text{-}Sc^{3+}\}^{3+}$ (**2**-Sc) was also investigated in C−H bond activation reactions. The C−H bond activation reactions by **2**-Sc were carried out with substrates having a weak C−H bond dissociation energy (BDE), such as xanthene (75.5 kcal $mol^{-1}$), 9,10-dihydroanthracene (DHA) (77.0 kcal $mol^{-1}$), 1,4-cyclohexadiene

(CHD) (78.0 kcal mol$^{-1}$), and fluorene (80.0 kcal mol$^{-1}$),[41] in $CH_3CN$ at −40 °C. Upon addition of xanthene (1.0 mM) to an $CH_3CN$ solution of **2**-Sc (0.10 mM) at −40 °C, the absorption band at 615 nm due to **2**-Sc decreased to give a first-order rate constant ($k_{obs}$) of $6.5 \times 10^{-1}$ s$^{-1}$, which was measured by the stopped-flow technique (Figure S19 in the Supporting Information); it is noted that **1** and **1**-Sc did not react with these substrates under the reaction conditions. The $k_{obs}$ value was in proportion to the xanthene concentration to give a second-order rate constant ($k_2$) of $6.6 \times 10^2$ M$^{-1}$ s$^{-1}$ in $CH_3CN$ at −40 °C (Figure S20a in the Supporting Information). The $k_2'$ values, which are calculated by dividing the $k_2$ value by the number of equivalent target C−H bonds of substrates, decrease with an increase in the C−H BDE values of the substrate, exhibiting a good linear correlation between the rate constants and the BDE values of the substrates (Figure 10a). In addition, a kinetic isotope effect (KIE) value of 5.1 was obtained in the oxidation of xanthene-$h_2$ and xanthene-$d_2$ in $CH_3CN$ at −40 °C (Figure 10b). The large KIE value and the good linear correlation between the $k_2'$ values and the C−H BDE values of substrates indicate that the C−H bond activation reaction occurs via an H atom abstraction process, which is the rate-determining step. A product analysis of the xanthene oxidation by **2**-Sc revealed the formation of xanthone as a major product (~80% yield) and $[Cr^V(O)(TAML)]^-$ as the decay product of **2**-Sc (Figure S21 in the Supporting Information). In conclusion, while **1** and **1**-Sc are inactive in H atom abstraction reactions, **2**-Sc shows a moderate reactivity in the C−H bond activation reactions (Figure S15b,d in the Supporting Information).[11a,42]

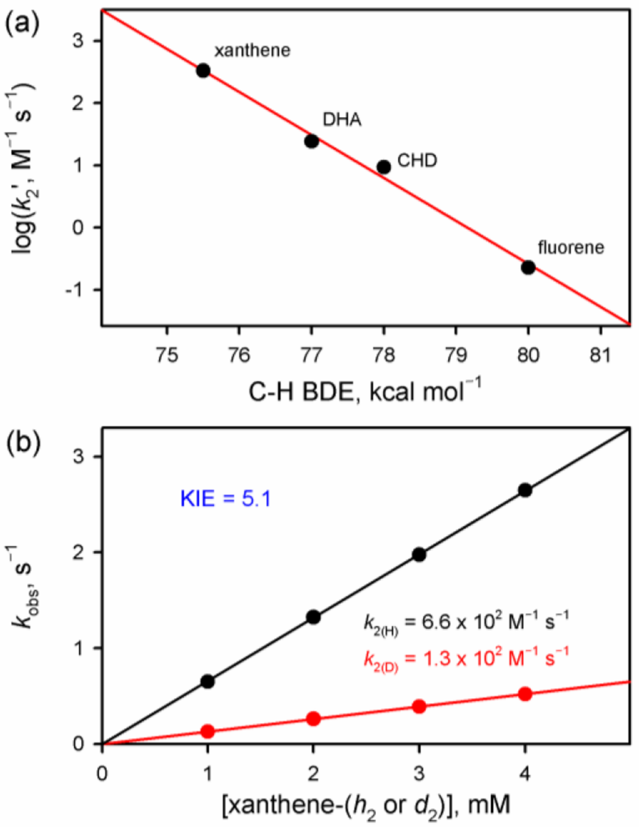

**Figure 10.** (a) Plot of log $k_2'$ against C−H BDE of substrates in the C−H bond activation reactions by **2**-Sc in $CH_3CN$ at −40 °C. The $k_2$ values were determined and adjusted for the reaction stoichiometry to yield the $k_2'$ values on the basis of the number of equivalent target C−H bonds of substrates. (b) Plots of the pseudo-first-order rate constants ($k_{obs}$) against the concentrations of xanthene-$h_2$ (black circles) and xanthene-$d_2$ (red circles) for the oxidation of xanthene-$h_2$ and xanthene-$d_2$ by **2**-Sc in $CH_3CN$ at −40 °C.

## CONCLUSION

A formal Cr(VI)−oxo complex binding Sc$^{3+}$ ion, $\{[Cr^V(O)(TAML^{\bullet+})]\text{-}Sc^{3+}\}^{3+}$, was synthesized and characterized with various spectroscopic techniques and DFT calculations, affording a geometric structure with Cr≡O triple-bond character and the binding Sc$^{3+}$ ion at the supporting TAML ligand. The $\{[Cr^V(O)(TAML^{\bullet+})]\text{-}Sc^{3+}\}^{3+}$ complex exhibits an extremely high ET reactivity toward one-electron donors, such as $[Fe^{II}(phen)_3]^{2+}$, with a reorganization energy of ET of 0.26 eV, which is the smallest λ value ever reported in the ET reactions of organic and inorganic oxidants, including high-valent metal−oxo complexes. By comparison of the sluggish reactivity of the precursors of the $\{[Cr^V(O)(TAML^{\bullet+})]\text{-}Sc^{3+}\}^{3+}$ complex, which are one less oxidized species and/or no Sc$^{3+}$ ion binding occurs, such as $[Cr^V(O)(TAML)]^-$ and $\{[Cr^V(O)(TAML)]\text{-}Sc^{3+}\}^{2+}$, the present results demonstrate how the oxidizing capability of high-valent metal−oxo species can be enhanced dramatically by increasing the oxidation state of the metal−oxo species and utilizing redox-inactive metal ions in catalytic oxidation reactions.

## EXPERIMENTAL SECTION

**Materials.** All chemicals, obtained from Aldrich Chemical Co. and Tokyo Chemical Industry, were of the best available purity and were used without further purification unless otherwise indicated. Solvents were dried according to published procedures and distilled under argon prior to use.[43] TAML-$H_4$ (TAML$^{4-}$ = 3,4,8,9-tetrahydro-3,3,6,6,9-hexamethyl-1*H*-1,4,8,11-benzotetraazocyclotridecane-2,5,7,10-(6*H*,11*H*)-tetrone; tetraamido macrocyclic ligand) was purchased from GreenOx Catalyst, Inc. (Pittsburgh, PA, USA). The starting Cr(III) complex, $Li[Cr^{III}(TAML)]$, was prepared according to the literature.[20a] The deuterated xanthene was synthesized by a literature method.[44] A purity of >99% deuteration was confirmed by $^1$H NMR. $H_2{}^{18}O$ (95% $^{18}$O-enriched) was supplied from Berry & Associates/ICON Isotopes.

**Instrumentation.** UV−vis spectra were recorded on a Hewlett-Packard 8453 diode array spectrophotometer equipped with a UNISOKU Scientific Instruments USP-203A Cryostat for low-temperature experiments or on a UNISOKU RSP-601 stopped-flow spectrometer equipped with a MOS-type highly sensitive photodiode array detector. Nanosecthe ond time-resolved transient absorption measurements were performed using an Nd:YAG laser as follows. A solution mixture in a quartz cell (1.0 cm × 1.0 cm) was excited by a Nd:YAG laser (Continuum SLII-10, 4−6 ns fwhm, $\lambda_{ex}$ = 355 nm, 80 mJ pulse$^{-1}$, 10 Hz). The photodynamics were monitored by continuous exposure to a xenon lamp for the visible region and a halogen lamp for near-IR region as probe lights and a photomultiplier tube (Hamamatsu 2949) as a detector. The kinetic traces at appropriate wavelengths were assembled from the time-resolved spectral data. EPR spectra were recorded at 77 K with use of a JEOL X-band spectrometer (JES-FA100). The *g* value was calibrated using the $Mn^{2+}$ marker. Cold spray ionization time-of-flight mass (CSI-MS) spectra were collected on a JMS-T100CS (JEOL) mass spectrometer equipped with a CSI source (typical measurement conditions: needle voltage 2.2 kV, orifice 1 current 50−500 nA, orifice 1 voltage 0−20 V, ringlens voltage 10 V, ion source temperature 5 °C, and spray temperature −40 °C). Resonance Raman (rRaman) spectral data were collected with a UniDRON (UniNanoTech, Korea) Microscope Raman chamber with a 20× long working objective lens and SR500i-A Raman spectrometer in combination with a DU420A-BU2 (ANDOR, UK) TE cooled CCD detector, cooled to −45 °C. An excitation wavelength of 441.7 nm was provided by a He-Cd laser (Kimmon Koha, IK5751I-G, Japan) with 20 mW power at the sample point. The laser beam was focused using an objective lens with a magnifying power of 10. The sample solution in an NMR tube was put into a 150 mL large quartz Dewar flasks (inner diameter 5.4 mm, outer diameter 10.5 mm, CortecNet, France), the data acquisition time was normally 10 s, and the data were accumulated for 12 times. Electrochemical measurements were performed on a CHI630B electrochemical analyzer in a deaerated $CH_3CN$ solution containing 0.10 M $n$-$Bu_4NPF_6$ ($TBAPF_6$) as the supporting electrolyte at 298 K. A conventional three-electrode cell was used with a platinum working electrode (surface area of 0.3 $mm^2$), a platinum wire as a counter electrode, and an $Ag/AgNO_3$ (0.010 M) electrode as a reference electrode. The platinum working electrode was routinely polished with a BAS polishing alumina suspension and rinsed with $CH_3CN$ before use. The measured potentials were recorded with respect to an $Ag/Ag^+$ reference electrode. All potentials (vs $Ag/Ag^+$) were converted to values vs SCE by adding 0.29 V.[45] $^1H$ NMR spectra were measured with a Bruker digital AVANCE III 400 FT-NMR spectrometer.

**Synthesis of 1, 1-Sc, and 2-Sc.** The chromium(V)−oxo complex $[Cr^V(O)(TAML)]^-$ (**1**) was generated by $O_2$ activation with the chromium(III) complex $[Cr^{III}(TAML)]^-$.[20] First, the $Li[Cr^{III}(TAML)]$ complex was synthesized by the reaction of $Cr^{II}(Cl)_2$ (1.0 mmol) with a tetradentate TAML-$H_4$ ligand (200 mg; 0.50 mmol) and lithium bis(trimethylsilyl)amide solution (2.7 mL, 1.0 M in THF) under an Ar atmosphere in THF at 25 °C.[20a] When the reaction solution was stirred for 30 min in the presence of $O_2$, a dark brown solution was formed that was stirred overnight at ambient temperature. The resulting brown solution was filtered, and the filtrate was evaporated to remove the solvent. The cation exchange from $Li^+$ ion to $PPh_4{}^+$ ion was performed by adding 10 equiv of $PPh_4Cl$ to a $CH_3CN/H_2O$ (v/v 20/1) solution of $Li[Cr^V(O)(TAML)]$ in order to increase the solubility of $[Cr^V(O)(TAML)]^-$ in $CH_3CN$. The reaction solution was filtered and used for further characterization studies. Single crystals of $(PPh_4)[Cr^V(O)(TAML)]$ (**1**-$PPh_4$) were obtained by slow diffusion of dried $Et_2O$ into a concentrated $CH_3CN$ solution of **1**-$PPh_4$ at −20 °C.

$\{[Cr^V(O)(TAML)]\text{-}Sc^{3+}\}^{2+}$ (**1**-Sc) was generated by addition of 5 equiv of $Sc(OTf)_3$ ($OTf^- = CF_3SO_3{}^-$) to a $CH_3CN$ solution of **1** at 25 °C. $\{[Cr^V(O)(TAML^{\bullet+})]\text{-}Sc^{3+}\}^{3+}$ (**2**-Sc) was generated by reacting **1**-Sc with a one-electron oxidant, such as $[Ru^{III}(bpy)_3]^{3+}$ and cerium(IV) ammonium nitrate (CAN), in $CH_3CN$ at −40 °C. Typically, the one-electron oxidant $[Ru^{III}(bpy)_3]^{3+}$ ($E_{red}$ vs SCE = 1.24 V) was added to a $CH_3CN$ solution of **1**-Sc (i.e., $[Cr^V(O)(TAML)]^-$ (**1**) in the presence of $Sc^{3+}$ ion) at −40 °C, resulting in an immediate color change from brown to dark green due to the formation of the one-electron-oxidized species of **1**-Sc (i.e., **2**-Sc).

For the complex $[Cr^V(^{18}O)(TAML)]^-$ (**1**-$^{18}O$), $^{18}O_2$ gas was applied to a THF solution of the $[Cr^{III}(TAML)]^-$ complex and the mixture was stirred for 12 h at 25 °C. **1**-Sc-$^{18}O$ and **2**-Sc-$^{18}O$ were generated by use of **1**-$^{18}O$ according to the procedures described above.

**EXAFS Measurements.** X-ray absorption spectra were collected at the Advanced Photon Source (APS) at Argonne National Laboratory on bending magnet beamline 20. The radiation was monochromatized by a Si(110) crystal monochromator. The intensity of the X-rays was monitored by three ion chambers (I0, I1, and I2) filled with 20% nitrogen and 80% helium and placed before the sample (I0) and after the sample (I1 and I2). Cr foil was placed between I1 and I2, and its absorption was recorded with each scan for energy calibration. Plastic (Lexan) EXAFS sample holders (inner dimensions of 12 mm × 2 mm × 3 mm) filled with frozen solutions were inserted into a cryostat precooled to 20 K. The samples were kept at 20 K under a He atmosphere at ambient pressure. Data were recorded as fluorescence excitation spectra using a 13-element Ge energy-resolving detector. In order to reduce the risk of sample damage by X-rays, a defocused mode (beam size 1 × 2 mm) was used and no damage was observed. The shutter was synchronized with the scan software, preventing exposure to X-rays between scans and during spectrometer movements.

**EXAFS Data Analysis.** Athena software was used for data processing.[46] The energy scale for each scan was normalized using Cr foil, and scans for same samples were added. Data in energy space were pre-edge corrected, normalized, and background corrected. The processed data were converted to the photoelectron wave vector ($k$) space and weighted by $k^3$. The electron wavenumber is defined as in eq 7

$$k = [\{2m(E - E_0)\}/\hbar^2]^{1/2} \tag{7}$$

where $E_0$ is the threshold energy. $k$-space data were truncated near zero crossings and Fourier-transformed into $R$-space. Artemis software was used for curve fitting. In order to fit the data, the Fourier peaks were isolated separately or the entire experimental spectrum was fitted. The individual Fourier peaks were isolated by applying a Hanning window. Curve fitting was performed using *ab initio* calculated phases and amplitudes from the FEFF8 program from the University of Washington. *Ab initio* calculated phases and amplitudes were used in the EXAFS equation (eq 8)[47]

$$\chi(k) = S_0^2 \sum \frac{N_j}{kR_j^2} f_{\mathrm{eff},j}(\pi, k, R_j) e^{-2\sigma_j^2 k^2} e^{-2R_j/\lambda_j(k)} \sin(2kR_j + \varphi_{ij}(k)) \tag{8}$$

where $N_j$ is the number of atoms in the $j$th shell, $R_j$ is the distance between the absorbing atoms and the atoms in the $j^{th}$ shell; $f_{\mathrm{eff},j}$ is the *ab initio* amplitude function for $j$, and $e^{-2\sigma_j^2 k^2}$ is the Debye−Waller factor for shell $j$ accounting for damping due to thermal and static disorder in the shell. The mean free path term ($e^{-2R_j/\lambda_j(k)}$) accounts for losses due to inelastic scattering. The oscillations in the EXAFS spectrum are reflected in the $\sin(2kR_j + \varphi_{ij}(k))$ term, where $\varphi_{ij}(k)$ is the *ab initio* phase function for the shell $j$. $S_0$ is an amplitude reduction factor. The EXAFS equation was used to fit experimental data using $N$, $E_0$, $R$, and $\sigma^2$ as variable parameters, while $S_0$ was kept fixed. The quality of the fit was evaluated by the $R$ factor: if the $R$ factor was less than 2%, then the fit was good enough. The reduced $\chi^2$ was used to justify the addition of new absorber−backscatter shells.

**X-ray Structural Analysis.** Single crystals of **1**-$PPh_4$ suitable for X-ray crystallographic analysis were obtained by slow diffusion of $Et_2O$ into a saturated $CH_3CN$ solution of **1**-$PPh_4$. These crystals were taken from the solution by a nylon loop (Hampton Research Co.) on a handmade copper plate and mounted on a goniometer head in a $N_2$ cryostream. The diffraction data for **1**-$PPh_4$ were collected at 100 K on a Bruker SMART AXS diffractometer equipped with a monochromator in the Mo K$\alpha$ ($\lambda$ = 0.71073 Å) incident beam. The CCD data were integrated and scaled using the Bruker-SAINT software package, and the structure was solved and refined using SHELXTL V 6.12.[48] Hydrogen atoms were located in calculated positions. The crystallographic data and selected bond distances and angles for **1**-$PPh_4$ are given in Tables S2 and S3 in the Supporting Information. In addition, CCDC-2005460 contains the supplementary crystallographic data for this paper.

**Kinetic Measurements and Product Analysis.** Nanosecond laser-induced transient absorption measurements were performed to examine the fast ET from the electron donors ($[Fe^{II}(5\text{-}Cl\text{-}phen)_3]^{2+}$, $[Fe^{II}(Ph_2\text{-}phen)_3]^{2+}$, and $[Fe^{II}(phen)_3]^{2+}$) to **2**-Sc. **2**-Sc was generated *in situ* by ET from **1**-Sc to the triplet excited state of 2,3-dichloro-5,6-dicyano-*p*-benzoquinone ($^3$DDQ*), where the transient absorption band due to $DDQ^{\bullet-}$ ($\lambda_{max}$ = 590 nm) and the absorption band due to **2**-Sc ($\lambda_{max}$ = 615 nm) were observed upon laser photoexcitation. Then electron transfer from the one-electron donor to **2**-Sc was monitored by the decay of absorbance at 615 nm due to **2**-Sc.

The sulfoxidation of *para*-substituted thioanisole derivatives (i.e., *para*-Cl-thioanisole, *para*-Br-thioanisole, *para*-CN-thioanisole, and *para*-$NO_2$-thioanisole) by **2**-Sc was also investigated using a stopped-flow spectrophotometer in $CH_3CN$ at −40 °C. Upon addition of thioanisole derivatives to an $CH_3CN$ solution of **2**-Sc at −40 °C, the decay of the absorption band at 615 nm due to **2**-Sc was monitored to determine the first-order rate constant ($k_{obs}$). The second-order rate constant ($k_2$) was determined from the slope of a linear plot of $k_{obs}$ vs concentration of a thioanisole derivative at −40 °C.

Kinetic measurements were also performed on a Hewlett-Packard 8453 photodiode-array spectrophotometer at −40 °C for C−H bond activation reactions. Xanthene, 9,10-dihydroanthracene (DHA), 1,4-cyclohexadiene, fluorene, and deuterated xanthene (xanthene-$d_2$) were used as substrates in the C−H bond activation reactions. Reactions were run in a 1.0 cm UV cuvette, with monitoring of the UV−vis spectral changes of reaction solutions. Rate constants were determined under pseudo-first-order conditions (e.g. [substrate]/[**2**-Sc] > 10) by fitting the absorbance changes at 615 nm due to **2**-Sc.

Products formed in the C−H bond activation of xanthene by **2**-Sc were analyzed by GC. Decane (1.0 mM) was used as an internal standard. Xanthene (10 mM) was added directly to a solution of **2**-Sc (1.0 mM), and then the mixture was stirred for 30 min at −40 °C. Xanthone was obtained as a major product with over 80% yield (based on the amount of **2**-Sc generated). Products formed in the oxygen transfer reaction from **2**-Sc to thioanisole were analyzed by HPLC. Thioanisole (10 mM) was added directly to a solution of **2**-Sc (1.0 mM), and then the mixture was stirred for 30 min at −40 °C. Methyl phenyl sulfoxide (PhS(=O)Me) was obtained as the major product with over 85% yield (based on the amount of **2**-Sc generated). The decay product of **2**-Sc analyzed with UV−vis, ESI-MS, and EPR spectroscopy was **1**-Sc.

**DFT Calculations.** Density functional theory calculations were carried out using the Gaussian 09 software program.[49] The geometry optimization was performed at the B3LYP/def2-SVP level.[50,51] Frequency calculations on the optimized geometries performed to confirm the nature of the stationary points were carried out at the same level of theory used for geometry optimization. Single-point energy evaluations were also done using a triple-$\zeta$ basis set: i.e., def2-TZVPP.[51] The conductor-like polarizable continuum model (CPCM) with UFF cavity,[52] per G09 default, was used to include the solvent (acetonitrile) effects in all of the calculations. Dispersion was included using the DFT-D3 program.[53]

## ■ ASSOCIATED CONTENT

### Supporting Information

The Supporting Information is available free of charge at https://pubs.acs.org/doi/10.1021/acscatal.1c00079.

Figures and tables as described in the text (PDF)
Crystallographic data (CIF)

## ■ AUTHOR INFORMATION

### Corresponding Authors

**Yulia Pushkar** − *Department of Physics and Astronomy, Purdue University, West Lafayette, Indiana 47907, United States;* orcid.org/0000-0001-7949-6472; Email: ypushkar@purdue.edu

**Shunichi Fukuzumi** − *Department of Chemistry and Nano Science, Ewha Womans University, Seoul 03760, Korea;* orcid.org/0000-0002-3559-4107; Email: fukuzumi@chem.eng.osaka-u.ac.jp

**Wonwoo Nam** − *Department of Chemistry and Nano Science, Ewha Womans University, Seoul 03760, Korea; School of Chemistry and Chemical Engineering, Shaanxi Normal University, Xi'an, People's Republic of China;* orcid.org/0000-0001-8592-4867; Email: wwnam@ewha.ac.kr

### Authors

**Young Hyun Hong** − *Department of Chemistry and Nano Science, Ewha Womans University, Seoul 03760, Korea;* orcid.org/0000-0001-8190-4156

**Yuri Jang** − *Department of Chemistry and Nano Science, Ewha Womans University, Seoul 03760, Korea*

**Roman Ezhov** − *Department of Physics and Astronomy, Purdue University, West Lafayette, Indiana 47907, United States;* orcid.org/0000-0001-6806-4033

**Mi Sook Seo** − *Department of Chemistry and Nano Science, Ewha Womans University, Seoul 03760, Korea;* orcid.org/0000-0003-3302-2508

**Yong-Min Lee** − *Department of Chemistry and Nano Science, Ewha Womans University, Seoul 03760, Korea;* orcid.org/0000-0002-5553-1453

**Bhawana Pandey** − *Department of Chemistry and Nano Science, Ewha Womans University, Seoul 03760, Korea*

**Seungwoo Hong** − *Department of Chemistry, Sookmyung Women's University, Seoul 04310, Korea;* orcid.org/0000-0001-7953-8433

Complete contact information is available at:

https://pubs.acs.org/10.1021/acscatal.1c00079

### Author Contributions

$^{\perp}$Y.H.H. and Y.J. contributed equally to this work.

### Notes

The authors declare no competing financial interest.

## ■ ACKNOWLEDGMENTS

This work was supported by the NRF of Korea through CRI (NRF-2012R1A3A2048842 to W.N.) and Basic Science Research Program (2020R1I1A1A01074630 to Y.-M.L., 2019R1I1A1A01055822 to M.S.S., and 2020R1A6A3A13072451 to Y.H.H.). This research was also supported by the NSF, CHE-1900476 (Y.P.), and Xi'an Key Laboratory of Organometallic Material Chemistry (W.N.). The use of the Advanced Photon Source, an Office of Science User Facility operated by the U.S. Department of Energy (DOE) Office of Science by Argonne National Laboratory, was supported by the U.S. DOE under Contract DE-AC02-06CH11357. The PNC/XSD (Sector 20) facilities at the Advanced Photon Source and research at these facilities were supported by the U.S. Department of Energy, Basic Energy Science, and the Canadian Light Source.

## ■ REFERENCES

(1) (a) Ortiz de Montellano, P. R. Hydrocarbon Hydroxylation by Cytochrome P 450 Enzymes. *Chem. Rev.* **2010**, *110*, 932−948. (b) Poulos, T. L. Heme Enzyme Structure and Function. *Chem. Rev.* **2014**, *114*, 3919−3962. (c) Guengerich, F. P. Mechanisms of Cytochrome P450-Catalyzed Oxidations. *ACS Catal.* **2018**, *8*, 10964−10976. (d) Mak, P. J.; Denisov, I. G. Spectroscopic Studies of the Cytochrome P450 Reaction Mechanisms. *Biochim. Biophys. Acta, Proteins Proteomics* **2018**, *1866*, 178−204. (e) Dubey, K. D.; Shaik, S. Cytochrome P450—The Wonderful Nanomachine Revealed through Dynamic Simulations of the Catalytic Cycle. *Acc. Chem. Res.* **2019**, *52*, 389−399.

(2) (a) Baglia, R. A.; Zaragoza, J. P. T.; Goldberg, D. P. Biomimetic Reactivity of Oxygen-Derived Manganese and Iron Porphyrinoid Complexes. *Chem. Rev.* **2017**, *117*, 13320−13352. (b) Huang, X.; Groves, J. T. Oxygen Activation and Radical Transformations in Heme Proteins and Metalloporphyrins. *Chem. Rev.* **2018**, *118*, 2491−2553. (c) Pereira, M. M.; Dias, L. D.; Calvete, M. J. F. Metalloporphyrins: Bioinspired Oxidation Catalysts. *ACS Catal.* **2018**, *8*, 10784−10808.

(3) (a) Rittle, J.; Green, M. T. Cytochrome P450 Compound I: Capture, Characterization, and C-H Bond Activation Kinetics. *Science* **2010**, *330*, 933−937. (b) Yosca, T. H.; Rittle, J.; Krest, C. M.; Onderko, E. L.; Silakov, A.; Calixto, J. C.; Behan, R. K.; Green, M. T. Iron(IV)hydroxide p$K_a$ and the Role of Thiolate Ligation in C−H Bond Activation by Cytochrome P450. *Science* **2013**, *342*, 825−829. (c) Yosca, T. H.; Ledray, A. P.; Ngo, J.; Green, M. T. A New Look at the Role of Thiolate Ligation in Cytochrome P450. *JBIC, J. Biol. Inorg. Chem.* **2017**, *22*, 209−220. (d) Mittra, K.; Green, M. T. Reduction Potentials of P450 Compounds I and II: Insight into the Thermodynamics of C-H Bond Activation. *J. Am. Chem. Soc.* **2019**, *141*, 5504−5510.

(4) (a) Nam, W. High-Valent Iron(IV)−Oxo Complexes of Heme and Non-Heme Ligands in Oxygenation Reactions. *Acc. Chem. Res.* **2007**, *40*, 522−531. (b) Guo, M.; Corona, T.; Ray, K.; Nam, W. Heme and Nonheme High-Valent Iron and Manganese Oxo Cores in Biological and Abiological Oxidation Reactions. *ACS Cent. Sci.* **2019**, *5*, 13−28.

(5) (a) Ishimizu, Y.; Ma, Z.; Hada, M.; Fujii, H. Experimental and Theoretical Studies of the Porphyrin Ligand Effect on the Electronic Structure and Reactivity of Oxoiron(IV) Porphyrin π-Cation-Radical Complexes. *JBIC, J. Biol. Inorg. Chem.* **2019**, *24*, 483−494. (b) Morimoto, Y.; Shimaoka, Y.; Ishimizu, Y.; Fujii, H.; Itoh, S. Direct Observation of Primary C-H Bond Oxidation by an Oxido-Iron(IV) Porphyrin π-Radical Cation Complex in a Fluorinated Carbon Solvent. *Angew. Chem., Int. Ed.* **2019**, *58*, 10863−10866. (c) Yokota, S.; Fujii, H. Critical Factors in Determining the Heterolytic versus Homolytic Bond Cleavage of Terminal Oxidants by Iron(III) Porphyrin Complexes. *J. Am. Chem. Soc.* **2018**, *140*, 5127−5137. (d) Asaka, M.; Fujii, H. Participation of Electron Transfer Process in Rate-Limiting Step of Aromatic Hydroxylation Reactions by Compound I Models of Heme Enzymes. *J. Am. Chem. Soc.* **2016**, *138*, 8048−8051.

(6) (a) Fukuzumi, S. Electron-Transfer Properties of High-Valent Metal-Oxo Complexes. *Coord. Chem. Rev.* **2013**, *257*, 1564−1575. (b) Fukuzumi, S.; Cho, K.-B.; Lee, Y.-M.; Hong, S.; Nam, W. Mechanistic Dichotomies in Redox Reactions of Mononuclear Metal-Oxygen Intermediates. *Chem. Soc. Rev.* **2020**, *49*, 8988−9027.

(7) Fukui, N.; Li, X.-X.; Nam, W.; Fukuzumi, S.; Fujii, H. Small Reorganization Energy for Ligand-Centered Electron-Transfer Reduction of Compound I to Compound II in a Heme Model Study. *Inorg. Chem.* **2019**, *58*, 8263−8266.

(8) (a) Devi, T.; Lee, Y.-M.; Nam, W.; Fukuzumi, S. Metal Ion-Coupled Electron-Transfer Reactions of Metal-Oxygen Complexes. *Coord. Chem. Rev.* **2020**, *410*, 213219. (b) Fukuzumi, S.; Lee, Y.-M.; Nam, W. Acid Catalysis via Acid-Promoted Electron Transfer. *Bull. Korean Chem. Soc.* **2020**, *41*, 1217−1232. (c) Nam, W.; Lee, Y.-M.; Fukuzumi, S. Hydrogen Atom Transfer Reactions of Mononuclear Nonheme Metal−Oxygen Intermediates. *Acc. Chem. Res.* **2018**, *51*, 2014−2022. (d) Fukuzumi, S.; Ohkubo, K.; Lee, Y.-M.; Nam, W. Lewis Acid Coupled Electron Transfer of Metal−Oxygen Intermediates. *Chem. - Eur. J.* **2015**, *21*, 17548−17559. (e) Nam, W.; Lee, Y.-M.; Fukuzumi, S. Tuning Reactivity and Mechanism in Oxidation Reactions by Mononuclear Nonheme Iron(IV)-Oxo complexes. *Acc. Chem. Res.* **2014**, *47*, 1146−1154.

(9) (a) Lee, Y.-M.; Kotani, H.; Suenobu, T.; Nam, W.; Fukuzumi, S. Fundamental Electron-Transfer Properties of Non-heme Oxoiron(IV) Complexes. *J. Am. Chem. Soc.* **2008**, *130*, 434−435. (b) Bataineh, H.; Pestovsky, O.; Bakac, A. Electron Transfer Reactivity of the Aqueous Iron(IV)−Oxo Complex. Outer-Sphere vs Proton-Coupled Electron Transfer. *Inorg. Chem.* **2016**, *55*, 6719−6724. (c) Comba, P.; Fukuzumi, S.; Kotani, H.; Wunderlich, S. Electron-Transfer Properties of an Efficient Nonheme Iron Oxidation Catalyst with a Tetradentate Bispidine Ligand. *Angew. Chem., Int. Ed.* **2010**, *49*, 2622−2625. (d) Comba, P.; Fukuzumi, S.; Koke, C.; Martin, B.; Löhr, A.-M.; Straub, J. A Bispidine Iron(IV)−Oxo Complex in the Entatic State. *Angew. Chem., Int. Ed.* **2016**, *55*, 11129−11133.

(10) (a) Yoon, H.; Lee, Y.-M.; Wu, X.; Cho, K.-B.; Sarangi, R.; Nam, W.; Fukuzumi, S. Enhanced Electron-Transfer Reactivity of Nonheme Manganese(IV)-Oxo Complexes by Binding Scandium Ions. *J. Am. Chem. Soc.* **2013**, *135*, 9186−9194. (b) Chen, J.; Yoon, H.; Lee, Y.-M.; Seo, M. S.; Sarangi, R.; Fukuzumi, S.; Nam, W. Tuning the Reactivity of Mononuclear Nonheme Manganese(IV)-Oxo Complexes by Triflic Acid. *Chem. Sci.* **2015**, *6*, 3624−3632. (c) Lee, Y.-M.; Kim, S.; Ohkubo, K.; Kim, K.-H.; Nam, W.; Fukuzumi, S. Unified Mechanism of Oxygen Atom Transfer and Hydrogen Atom Transfer Reactions with a Triflic Acid-Bound Nonheme Manganese(IV)−Oxo Complex via Outer-Sphere Electron Transfer. *J. Am. Chem. Soc.* **2019**, *141*, 2614−2622. (d) Sankaralingam, M.; Lee, Y.-M.; Pineda-Galvan, Y.; Karmalkar, D. G.; Seo, M. S.; Jeon, S. H.; Pushkar, Y.; Fukuzumi, S.; Nam, W. Redox Reactivity of a Mononuclear Manganese-Oxo Complex Binding Calcium Ion and Other Redox-Inactive Metal Ions. *J. Am. Chem. Soc.* **2019**, *141*, 1324−1336. (e) Sharma, N.; Lee, Y.-M.; Li, X.-X.; Nam, W.; Fukuzumi, S. Singly Unified Driving Force Dependence of Outer-Sphere Electron-Transfer Pathways of Nonheme Manganese(IV)−Oxo Complexes in the Absence and Presence of Lewis Acids. *Inorg. Chem.* **2019**, *58*, 13761−13765. (f) Karmalkar, D. G.; Sankaralingam, M.; Seo, M. S.; Ezhov, R.; Lee, Y.-M.; Pushkar, Y. N.; Kim, W.-S.; Fukuzumi, S.; Nam, W. A High-Valent Manganese(IV)−Oxo−Cerium(IV) Complex and Its Enhanced Oxidizing Reactivity. *Angew. Chem., Int. Ed.* **2019**, *58*, 16124−16129.

(11) (a) Kotani, H.; Kaida, S.; Ishizuka, T.; Sakaguchi, M.; Ogura, T.; Shiota, Y.; Yoshizawa, K.; Kojima, T. Formation and Characterization of a Reactive Chromium(V)−Oxo Complex: Mechanistic Insight into Hydrogen-Atom Transfer Reactions. *Chem. Sci.* **2015**, *6*, 945−955. (b) Liu, S.; Jung, J.; Ohkubo, K.; Hicks, S. D.; Bougher, C. J.; Abu-Omar, M. M.; Fukuzumi, S. Activationless Electron Self-Exchange of High-Valent Oxo and Imido Complexes of Chromium Corroles. *Inorg. Chem.* **2015**, *54*, 9223−9228.

(12) Prokop, K. A.; Neu, H. M.; Visser, S. P.; Goldberg, D. P. A Manganese(V)-Oxo *π*-Cation Radical Complex: Influence of One-Electron Oxidation on Oxygen-Atom Transfer. *J. Am. Chem. Soc.* **2011**, *133*, 15874−15877.

(13) Karmalkar, D. G.; Li, X.-X.; Seo, M. S.; Sankaralingam, M.; Ohta, T.; Sarangi, R.; Hong, S.; Nam, W. A Manganese(V)-Oxo Tetraamido Macrocyclic Ligand (TAML) Cation Radical Complex: Synthesis, Characterization, and Reactivity Studies. *Chem. - Eur. J.* **2018**, *24*, 17927−17931.

(14) Shi, H.; Xie, J.; Lam, W. W. Y.; Man, W.-L.; Mak, C.-K.; Yiu, S. M.; Lee, H. K.; Lau, T.-C. Generation and Reactivity of a One-Electron-Oxidized Manganese(V) Imido Complex with a Tetraamido Macrocyclic Ligand. *Chem. - Eur. J.* **2019**, *25*, 12895−12899.

(15) (a) Lu, X.; Li, X.-X.; Lee, Y.-M.; Jang, Y.; Seo, M. S.; Hong, S.; Cho, K.-B.; Fukuzumi, S.; Nam, W. Electron-Transfer and Redox Reactivity of High-Valent Iron Imido and Oxo Complexes with the Formal Oxidation States of Five and Six. *J. Am. Chem. Soc.* **2020**, *142*, 3891−3904. (b) Hong, S.; Lu, X.; Lee, Y.-M; Seo, M. S.; Ohta, T.; Ogura, T.; Clemancey, M.; Maldivi, P.; Latour, J. M.; Sarangi, R.; Nam, W. Achieving One-Electron Oxidation of a Mononuclear Nonheme Iron(V)-Imido Complex. *J. Am. Chem. Soc.* **2017**, *139*, 14372−14375.

(16) Goto, Y.; Matsui, T.; Ozaki, S.; Watanabe, Y.; Fukuzumi, S. Mechanisms of Sulfoxidation Catalyzed by High-Valent Intermediates of Heme Enzymes: Electron-Transfer vs Oxygen-Transfer Mechanism. *J. Am. Chem. Soc.* **1999**, *121*, 9497−9502.

(17) (a) Czernuszewicz, R. S.; Mody, V.; Czader, A.; Gałęzowski, M.; Gryko, D. T. Why the Chromyl Bond Is Stronger Than the Perchromyl Bond in High-Valent Oxochromium(IV,V) Complexes of Tris(pentafluorophenyl)corrole. *J. Am. Chem. Soc.* **2009**, *131*, 14214−14215. (b) Cho, J.; Woo, J.; Han, J. E.; Kubo, M.; Ogura, T.; Nam, W. Chromium(V)-Oxo and Chromium(III)-Superoxo Complexes Bearing a Macrocyclic TMC Ligand in Hydrogen Atom Abstraction Reactions. *Chem. Sci.* **2011**, *2*, 2057−2062.

(18) (a) Meier-Callahan, A. E.; Gray, H. B.; Gross, Z. Stabilization of High-Valent Metals by Corroles: Oxo[tris(pentafluorophenyl)-corrolato]chromium(V). *Inorg. Chem.* **2000**, *39*, 3605−3607. (b) Fujii, H.; Yoshimura, T.; Kamada, H. ESR Studies of Oxochromium(V) Porphyrin Complexes: Electronic Structure of the $Cr^V{=}O$ Moiety. *Inorg. Chem.* **1997**, *36*, 1122−1127.

(19) Weare, W. W.; Pushkar, Y.; Yachandra, V. K.; Frei, H. Visible Light-Induced Electron Transfer from Di-*μ*-Oxo-Bridged Dinuclear Mn Complexes to Cr Centers in Silica Nanopores. *J. Am. Chem. Soc.* **2008**, *130*, 11355−11363.

(20) (a) Collins, T. J.; Slebodnick, C.; Uffelman, E. S. Chromium(V)-Oxo Complexes of Macrocyclic Tetraamido-*N* Ligands Tailored for Highly Oxidized Middle Transition Metal Complexes: A New $^{18}O$-Labeling Reagent and a Structure with Four Nonplanar Amides. *Inorg. Chem.* **1990**, *29*, 3433−3436. (b) Baglia, R. A.; Prokop-Prigge, K. A.; Neu, H. M.; Siegler, M. A.; Goldberg, D. P. Mn(V)(O) versus Cr(V)(O) Porphyrinoid Complexes: Structural Characterization and Implications for Basicity Controlling H-Atom Abstraction. *J. Am. Chem. Soc.* **2015**, *137*, 10874−10877.

(21) Ehudin, M. A.; Gee, L. B.; Sabuncu, S.; Braun, A.; Moënne-Loccoz, P.; Hedman, B.; Hodgson, K. O.; Solomon, E. I.; Karlin, K. D. Tuning the Geometric and Electronic Structure of Synthetic High-Valent Heme Iron(IV)-Oxo Models in the Presence of a Lewis Acid and Various Axial Ligands. *J. Am. Chem. Soc.* **2019**, *141*, 5942−5960.

(22) Hong, S.; Lee, Y.-M.; Sankaralingam, M.; Vardhaman, A. K.; Park, Y. J.; Cho, K.-B.; Ogura, T.; Sarangi, R.; Fukuzumi, S.; Nam, W. A Manganese(V)−Oxo Complex: Synthesis by Dioxygen Activation and Enhancement of Its Oxidizing Power by Binding Scandium Ion. *J. Am. Chem. Soc.* **2016**, *138*, 8523−8532.

(23) It should be noted that it is possible to oxidize **1** by one electron to **2**. However, it is difficult to oxidize to isolate the one-electron-oxidized species selectively by chemical oxidants (e.g. $[Ru^{III}(bpy)_3]^{3+}$ or CAN) because the one-electron-oxidation peak potential ($E_{pa}$ = 1.07 V vs SCE) and two-electron-oxidation peak potential ($E_{pa}$ = 1.21 V vs SCE) of **1** are quite close. In the case of **1**-Sc, the two-electron-oxidation peak shifted greatly in the positive direction, suggesting that only the one-electron-oxidized species can be obtained. Thus, this is the reason the $Sc^{3+}$ ion was used.

(24) Ohkubo, K.; Fujimoto, A.; Fukuzumi, S. Visible-Light-Induced Oxygenation of Benzene by the Triplet Excited State of 2,3-Dichloro-5,6-dicyano-*p*-benzoquinone. *J. Am. Chem. Soc.* **2013**, *135*, 5368−5371.

(25) Ohkubo, K.; Hirose, K.; Fukuzumi, S. Solvent-Free One-Step Photochemical Hydroxylation of Benzene Derivatives by the Singlet Excited State of 2,3-Dichloro-5,6-dicyano-*p*-benzoquinone Acting as a Super Oxidant. *Chem. - Eur. J.* **2015**, *21*, 2855−2861.

(26) (a) Marcus, R. A. Chemical and Electrochemical Electron-Transfer Theory. *Annu. Rev. Phys. Chem.* **1964**, *15*, 155−196. (b) Marcus, R. A. Electron Transfer Reactions in Chemistry: Theory and Experiment (Nobel Lecture). *Angew. Chem., Int. Ed. Engl.* **1993**, *32*, 1111−1121.

(27) (a) Chang, R. ESR Study of Organic Electron Transfer Reactions. *J. Chem. Educ.* **1970**, *47*, 563−568. (b) Cheng, K. S.; Hirota, N. In *Investigation of Rates and Mechanisms of Reactions*; Hammes, G. G., Ed.; Wiley-Interscience: New York, 1974; Vol. *VI*, p 565.

(28) Fukuzumi, S.; Nakanishi, I.; Suenobu, T.; Kadish, K. M. Electron-Transfer Properties of $C_{60}$ and *tert*-Butyl-$C_{60}$ Radical. *J. Am. Chem. Soc.* **1999**, *121*, 3468−3474.

(29) Fukuzumi, S.; Ohkubo, K.; Suenobu, T.; Kato, K.; Fujitsuka, M.; Ito, O. Photoalkylation of 10-Alkylacridinium Ion via a Charge-Shift Type of Photoinduced Electron Transfer Controlled by Solvent Polarity. *J. Am. Chem. Soc.* **2001**, *123*, 8459−8467.

(30) Capocasa, G.; Sessa, F.; Tavani, F.; Monte, M.; Olivo, G.; Pascarelli, S.; Lanzalunga, O.; Di Stefano, S.; D'Angelo, P. Coupled X-ray Absorption/UV−vis Monitoring of Fast Oxidation Reactions Involving a Nonheme Iron−Oxo Complex. *J. Am. Chem. Soc.* **2019**, *141*, 2299−2304.

(31) Mukherjee, G.; Alili, A.; Barman, P.; Kumar, D.; Sastri, C. V.; de Visser, S. P. Interplay Between Steric and Electronic Effects: A Joint Spectroscopy and Computational Study of Nonheme Iron(IV)-Oxo Complexes. *Chem. - Eur. J.* **2019**, *25*, 5086−5098.

(32) Seo, M. S.; Kim, N. H.; Cho, K.-B.; So, J. E.; Park, S. K.; Clémancey, M.; Garcia-Serres, R.; Latour, J.-M.; Shaik, S.; Nam, W. A Mononuclear Nonheme Iron(IV)-Oxo Complex Which Is More Reactive Than Cytochrome P450 Model Compound I. *Chem. Sci.* **2011**, *2*, 1039−1045.

(33) Wilson, S. A.; Chen, J.; Hong, S.; Lee, Y.-M.; Clémancey, M.; Garcia-Serres, R.; Nomura, T.; Ogura, T.; Latour, J.-M.; Hedman, B.; Hodgson, K. O.; Nam, W.; Solomon, E. I. $[Fe^{IV}{=}O(TBC)(CH_3CN)]^{2+}$: Comparative Reactivity of Iron(IV)-Oxo Species with Constrained Equatorial Cyclam Ligation. *J. Am. Chem. Soc.* **2012**, *134*, 11791−11806.

(34) We assume that the difference in the redox potential between −40 and 25 °C is negligible, because the difference in the redox potential of decamethylferrocenium cation/decamethylferrocene couple in $CH_3CN$ between −40 and 25 °C is ca. 0.02 V and the one-electron-reduction potentials of $[Fe^{IV}(O)(TMC)]^{2+}$ (TMC = 1,4,8,11-tetramethyl-1,4,8,11-tetraazacyclotetradecane) in $CH_3CN$ at −40 and 25 °C are identical. See: (a) Matsumoto, M.; Swaddle, T. W. The Decamethylferrocene(+/0) Electrode Reaction in Organic Solvents at Variable Pressure and Temperature. *Inorg. Chem.* **2004**, *43*, 2724. (b) Hong, S.; So, H.; Yoon, H.; Cho, K.-B.; Lee, Y.-M.; Fukuzumi, S.; Nam, W. *Dalton Trans.* **2013**, *42*, 7842.

(35) The reorganization energy for OAT from **2**-Sc to thioanisole derivatives means that for ET from **2**-Sc to thioanisole derivatives, which is the rate-determining step of the OAT reactions.

(36) Park, J.; Lee, Y.-M.; Nam, W.; Fukuzumi, S. Brønsted Acid-Promoted C−H Bond Cleavage via Electron Transfer from Toluene Derivatives to a Protonated Nonheme Iron(IV)-Oxo Complex with No Kinetic Isotope Effect. *J. Am. Chem. Soc.* **2013**, *135*, 5052.

(37) In outer-sphere ET involving coordinatively saturated metal complexes such as $[\mathrm{Fe^{III}(L)}]_3{}^{3+}$ in a polar solvent ($CH_3CN$), the work term is normally neglected (see ref 38). In the case of ET from **2**-Sc to organic molecules (i.e., thioanisole derivatives), however, the work term is not negligible to afford the much larger equilibrium constants of the precursor complexes formed prior to ET.

(38) (a) Fukuzumi, S. *Electron Transfer: Mechanisms and Applications*; Wiley-VCH: Weinheim, Germany, 2020. (b) Fukuzumi, S.; Wong, C. L.; Kochi, J. K. Unified View of Marcus Electron Transfer and Mulliken Charge Transfer Theories in Organometallic Chemistry. Steric Effects in Alkylmetals as Quantitative Probes for Outer-Sphere and Inner-Sphere Mechanisms. *J. Am. Chem. Soc.* **1980**, *102*, 2928−2939.

(39) It should be noted that the redox potentials of metal complexes of 3+/2+ couples as well as that of an organic cation of a 2+/1+ couple are known to be insensitive to the ionic strength at quite different concentrations of tetrabutylammonium perchlorate (see ref 40). As shown in Figure S12c, the second-order rate constants in the oxidation of *para*-CN-thioanisole by **2**-Sc in the absence and presence of tetrabutylammonium hexafluorophosphate ($n$-$Bu_4NPF_6$; 20 mM) in $CH_3CN$ at −40 °C are identical within error margin.

(40) Okamoto, K.; Ohkubo, K.; Kadish, K. M.; Fukuzumi, S. Remarkable Accelerating Effects of Ammonium Cations on Electron-Transfer Reactions of Quinones by Hydrogen Bonding with Semiquinone Radical Anions. *J. Phys. Chem. A* **2004**, *108*, 10405.

(41) Luo, Y.-R. *Handbook of Bond Dissociation Energies in Organic Compounds*; CRC Press: New York, 2002.

(42) Kotani, H.; Kaida, S.; Ishizuka, T.; Mieda, K.; Sakaguchi, M.; Ogura, T.; Shiota, Y.; Yoshizawa, K.; Kojima, T. Importance of the Reactant-State Potentials of Chromium(V)−Oxo Complexes to Determine the Reactivity in Hydrogen-Atom Transfer Reactions. *Inorg. Chem.* **2018**, *57*, 13929−13936.

(43) Armarego, W. L. F.; Chai, C. L. L. *Purification of Laboratory Chemicals*, 6th ed.; Pergamon Press: Oxford, 2009.

(44) (a) Goldsmith, C. R.; Jonas, R. T.; Stack, T. D. P. C-H Bond Activation by a Ferric Methoxide Complex: Modeling the Rate-Determining Step in the Mechanism of Lipoxygenase. *J. Am. Chem. Soc.* **2002**, *124*, 83−96. (b) Arunkumar, C.; Lee, Y.-M.; Lee, J. Y.; Fukuzumi, S.; Nam, W. Hydrogen-Atom Abstraction Reactions by Manganese(V)− and Manganese(IV)−Oxo Porphyrin Complexes in Aqueous Solution. *Chem. - Eur. J.* **2009**, *15*, 11482−11489.

(45) Mann, C. K.; Barnes, K. K. In *Electrochemical Reactions in Non-aqueous Systems*; Mercel Dekker: New York, 1970.

(46) Ravel, B.; Newville, M. J. ATHENA, ARTEMIS, HEPHAESTUS: Data Analysis for X-Ray Absorption Spectroscopy Using IFEFFIT. *J. Synchrotron Radiat.* **2005**, *12*, 537−541.

(47) Rehr, J. J.; Albers, R. C. Theoretical Approaches to X-Ray Absorption Fine Structure. *Rev. Mod. Phys.* **2000**, *72*, 621−654.

(48) Sheldrick, G. M. *SHELXTL/PC Version 6.12 for Windows XP*; Bruker AXS Inc.: Madison, WI, USA, 2001.

(49) Frisch, M. J.; Trucks, G. W.; Schlegel, H. B.; Scuseria, G. E.; Robb, M. A.; Cheeseman, J. R.; Scalmani, G.; Barone, V.; Mennucci, B.; Petersson, G. A.; Nakatsuji, H.; Caricato, M.; Li, X.; Hratchian, H. P.; Izmaylov, A. F.; Bloino, J.; Zheng, G.; Sonnenberg, J. L.; Hada, M.; Ehara, M.; Toyota, K.; Fukuda, R.; Hasegawa, J.; Ishida, M.; Nakajima, T.; Honda, Y.; Kitao, O.; Nakai, H.; Vreven, T.; Montgomery, J. A., Jr.; Peralta, J. E.; Ogliaro, F.; Bearpark, M.; Heyd, J. J.; Brothers, E.; Kudin, K. N.; Staroverov, V. N.; Keith, T.; Kobayashi, R.; Normand, J.; Raghavachari, K.; Rendell, A.; Burant, J. C.; Iyengar, S. S.; Tomasi, J.; Cossi, M.; Rega, N.; Millam, J. M.; Klene, M.; Knox, J. E.; Cross, J. B.; Bakken, V.; Adamo, C.; Jaramillo, J.; Gomperts, R.; Stratmann, R. E.; Yazyev, O.; Austin, A. J.; Cammi, R.; Pomelli, C.; Ochterski, J. W.; Martin, R. L.; Morokuma, K.; Zakrzewski, V. G.; Voth, G. A.; Salvador, P.; Dannenberg, J. J.; Dapprich, S.; Daniels, A. D.; Farkas, O.; Foresman, J. B.; Ortiz, J. V.; Cioslowski, J.; Fox, D. J. *Gaussian 09 rev. D.01*; Gaussian, Inc.: Wallingford, CT, 2013.

(50) (a) Becke, A. D. Density-Functional Thermochemistry. III. The Role of Exact Exchange. *J. Chem. Phys.* **1993**, *98*, 5648−5652. (b) Becke, A. D. Density-Functional Exchange-Energy Approximation with Correct Asymptotic Behavior. *Phys. Rev. A: At., Mol., Opt. Phys.* **1988**, *38*, 3098−3100. (c) Lee, C.; Yang, W.; Parr, R. G. Development of the Colle-Salvetti Correlation-Energy Formula into a Functional of the Electron Density. *Phys. Rev. B: Condens. Matter Mater. Phys.* **1988**, *37*, 785−789.

(51) Weigend, F.; Ahlrichs, R. Balanced Basis Sets of Split Valence, Triple Zeta Valence and Quadruple Zeta Valence Quality for H to Rn: Design and Assessment of Accuracy. *Phys. Chem. Chem. Phys.* **2005**, *7*, 3297−3305.

(52) Cossi, M.; Rega, N.; Scalmani, G.; Barone, V. Energies, Structures, and Electronic Properties of Molecules in Solution with the C-PCM Solvation Model. *J. Comput. Chem.* **2003**, *24*, 669−681.

(53) (a) Grimme, S.; Antony, J.; Ehrlich, S.; Krieg, H. A Consistent and Accurate *Ab Initio* Parametrization of Density Functional Dispersion Correction (DFT-D) for the 94 Elements H-Pu. *J. Chem. Phys.* **2010**, *132*, 154104. (b) Grimme, S.; Ehrlich, S.; Goerigk, L. Effect of the Damping Function in Dispersion Corrected Density Functional Theory. *J. Comput. Chem.* **2011**, *32*, 1456−1465.